



LINEAR AND NON-LINEAR PREPROCESSING  
OF WAVEFRONT SENSOR SLOPE MEASUREMENTS  
FOR IMPROVED ADAPTIVE OPTICS PERFORMANCE

DISSERTATION  
Dennis Anthony Montera  
Captain, USAF

AFIT/DS/ENG/96-03

**DISTRIBUTION STATEMENT A**

Approved for public release;  
Distribution Unlimited

**DTIC QUALITY INSPECTED 3**

DEPARTMENT OF THE AIR FORCE  
AIR UNIVERSITY  
**AIR FORCE INSTITUTE OF TECHNOLOGY**

Wright-Patterson Air Force Base, Ohio

AFIT/DS/ENG/96-03

LINEAR AND NON-LINEAR PREPROCESSING  
OF WAVEFRONT SENSOR SLOPE MEASUREMENTS  
FOR IMPROVED ADAPTIVE OPTICS PERFORMANCE

DISSERTATION  
Dennis Anthony Montera  
Captain, USAF

AFIT/DS/ENG/96-03

**DTIC QUALITY INSPECTED 3**

Approved for public release; distribution unlimited

19970317 026

AFIT/DS/ENG/96-03

LINEAR AND NON-LINEAR PREPROCESSING  
OF WAVEFRONT SENSOR SLOPE MEASUREMENTS  
FOR IMPROVED ADAPTIVE OPTICS PERFORMANCE

DISSERTATION

Presented to the Faculty of the Graduate School of Engineering  
of the Air Force Institute of Technology

Air University

In Partial Fulfillment of the  
Requirements for the Degree of  
Doctor of Philosophy

Dennis Anthony Montera, B.S.E.E., M.S.E.E.

Captain, USAF

19 March, 1996

Approved for public release; distribution unlimited

LINEAR AND NON-LINEAR PREPROCESSING  
OF WAVEFRONT SENSOR SLOPE MEASUREMENTS  
FOR IMPROVED ADAPTIVE OPTICS PERFORMANCE

Dennis Anthony Montera, B.S.E.E., M.S.E.E.

Captain, USAF

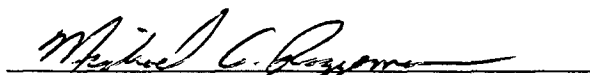
Approved:



Byron M. Welsh  
Chairman, Advisory Committee

21 Feb 96

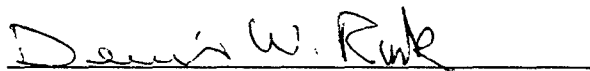
Date



Michael C. Roggemann, Major, USAF  
Member, Advisory Committee

21 Feb 96

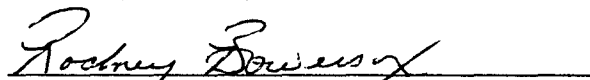
Date



Dennis W. Ruck, Major, USAF  
Member, Advisory Committee

21 FEB 96

Date

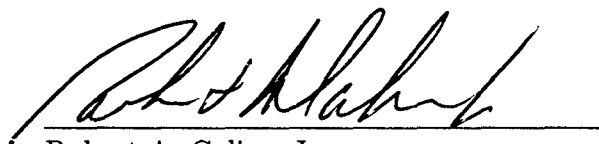


Rodney Bowersox  
Dean's Representative

21 Feb 96

Date

Accepted:



Robert A. Calico, Jr.  
Dean, Graduate School of Engineering

## *Acknowledgements*

What an assignment! These last three years at AFIT have truly been a wonderful experience. Not only has this been a tremendous learning experience, but I have met and worked with many wonderful people who have made this research a success. I would especially like to thank Dr. Byron Welsh, who gave me this opportunity, guided me with his insight, but also allowed me to find my own path. It has truly been my pleasure and my honor to work with you. I would like to thank my committee members Dr. Michael Roggemann and Dr. Dennis Ruck who always had time in their schedules to entertain my questions, and were always willing to give advice to help me along my way. I would like to acknowledge Dan Zambon and Dave Doak who managed to keep the computer systems up and running despite my research. I would like to thank Maj. Peter Raeth who volunteered his time and the Army Corps of Engineers Waterways Experiment Station for use of their Cray YMP8 computer resources, both of which helped me finish on time. I would also like to thank the Starfire Optical Range, Phillips Laboratory, Kirtland Air Force Base, New Mexico and the Air force Office of Scientific Research for supporting this effort.

Most importantly, I would like to thank my wife, Ilona, and my daughter, Marena, for all their support. Your love, sacrifice, and understanding are what truly made this research possible.

Dennis Anthony Montera

## *Table of Contents*

	Page
Acknowledgements . . . . .	iii
List of Figures . . . . .	vii
List of Tables . . . . .	ix
Abstract . . . . .	x
I. Introduction . . . . .	1
1.1 Limits on Adaptive Optics Performance . . . . .	2
1.2 Past Solutions . . . . .	3
1.3 Improving WFS Slope Measurement Accuracy . . . . .	4
1.3.1 WFS Slope Measurement Error . . . . .	5
1.3.2 System Time Delay . . . . .	8
1.4 Key Parameter Estimation . . . . .	10
1.5 Research Goals and Overview . . . . .	11
1.6 Dissertation Organization . . . . .	14
II. Data Generation . . . . .	15
2.1 WFS Slope Measurement Data Generation . . . . .	15
2.2 Phase Screen Data Generation . . . . .	19
III. Improving the WFS Estimated Slope Signal . . . . .	22
3.1 Reduction of WFS Slope Measurement Error . . . . .	22
3.1.1 Reduction of WFS Slope Measurement Error Through Slope Vector Processing . . . . .	22

	Page
3.1.2 Reduction of WFS Slope Measurement Error Within a Single WFS Subaperture . . . . .	30
3.2 WFS Slope Measurement Prediction . . . . .	40
IV. Key Parameter Estimation . . . . .	53
4.1 Estimation of $r_0$ . . . . .	53
4.2 Estimation of the Wind Speed Profile . . . . .	60
4.3 Estimation of the Relative Atmospheric Layer Strengths . . . . .	60
4.4 Estimation of WFS Mean Square Slope Estimation Error . . . . .	61
4.5 Key Parameter Estimation Summary . . . . .	64
V. Conclusions . . . . .	66
5.1 Individual Experiment Summaries . . . . .	66
5.1.1 Reducing WFS Mean Square Slope Estimation Error Through Processing a Frame of WFS Slope Measurements . . . . .	67
5.1.2 Reducing WFS Mean Square Slope Estimation Error Through Improving the Centroid Estimation Within a Single WFS Subaperture . . . . .	67
5.1.3 Compensating for System Time Delay . . . . .	67
5.1.4 Estimating $r_0$ . . . . .	68
5.1.5 Estimating the Wind Speed Profile . . . . .	68
5.1.6 Estimating the Strengths of the Atmospheric Turbulence Layers . . . . .	68
5.1.7 Estimating the WFS Mean Square Slope Estimation Error . . . . .	68
5.2 Conclusions on Overall Research Goals . . . . .	69
Appendix A. Development of Slope Covariance . . . . .	73
Appendix B. Development of Phase Covariance . . . . .	78
Appendix C. Phase covariance calculation: Gegenbauer polynomial technique . . . . .	83

	Page
Appendix D.      Development of the Lenslet SNR Ratio . . . . .	85
Bibliography . . . . .	88
Vita . . . . .	91

## *List of Figures*

Figure		Page
1.	Lenslet image on detector array when image main lobe is smaller than a single detector. . . . .	8
2.	WFS subaperture geometry. . . . .	17
3.	WFS slope measurement error reduction, fixed conditions, low measurement error. . . . .	24
4.	WFS slope measurement error reduction, fixed conditions, high measurement error. . . . .	25
5.	WFS slope measurement error reduction, variable conditions, neural network versus Bayes optimal solution, data with global tilt. . . . .	27
6.	WFS slope measurement error reduction, variable conditions, neural network, suboptimized Bayes solution, and Bayes optimal solution, data with global tilt. . . . .	28
7.	WFS slope measurement error reduction, variable conditions, neural network versus suboptimized Bayes solution, data with global tilt. . . . .	29
8.	Comparison of slope covariance with and without global tilt. . . . .	30
9.	WFS slope measurement error reduction, variable conditions, neural network versus Bayes optimal solution, data with global tilt removed. . . . .	31
10.	WFS slope measurement error reduction, variable conditions, neural network versus suboptimized Bayes solution, data with global tilt removed. . . . .	32
11.	Comparison of WFS lenslet centroid estimation on images with main lobe the width of a single detector and no noise. . . . .	34
12.	Comparison of WFS lenslet centroid estimation on images with main lobe the width of a single detector and SNR between 7.5 and 11.0. . . . .	35
13.	Comparison of WFS lenslet centroid estimation on images with main lobe the width of a single detector and SNR between 4.0 and 7.5. . . . .	36
14.	Comparison of WFS lenslet centroid estimation on images with main lobe half the width of a single detector and no noise. . . . .	37

Figure		Page
15.	Comparison of WFS lenslet centroid estimation on images with main lobe half the width of a single detector and SNR between 7.5 and 11.0. . . . .	38
16.	Comparison of WFS lenslet centroid estimation on images with main lobe half the width of a single detector and SNR between 4.0 and 7.5. . . . .	39
17.	Comparison of standard deviation about the mean in WFS lenslet centroid estimation. . . . .	41
18.	WFS slope prediction under fixed conditions, data with global tilt. . . . .	43
19.	WFS slope prediction under fixed conditions, data with global tilt removed. . . . .	44
20.	WFS slope prediction under variable conditions, data with global tilt. . . . .	46
21.	WFS slope prediction under variable conditions, data with global tilt removed. . . . .	47
22.	WFS slope prediction under variable conditions, data with global tilt removed, neural network versus fixed statistical predictor with wind speeds set at $0.0D$ per frame. . . . .	48
23.	WFS slope prediction under variable conditions, data with global tilt removed, neural network versus fixed statistical predictor with wind speeds set at $0.05D$ per frame. . . . .	49
24.	WFS slope prediction under variable conditions, data with global tilt removed, neural network versus fixed statistical predictor with wind speeds set at $0.1D$ per frame. . . . .	50
25.	WFS slope prediction under increased wind speed conditions. . . . .	51
26.	WFS slope prediction, 2 frames versus 3 frames as inputs. . . . .	51
27.	$D/r_0$ estimation with no WFS slope measurement error. . . . .	55
28.	$D/r_0$ estimation with WFS slope measurement error present, data with global tilt. . . . .	58
29.	$D/r_0$ estimation with WFS slope measurement error present, data with global tilt removed. . . . .	59
30.	WFS slope measurement error estimation, data with global tilt. . . . .	63
31.	WFS slope measurement error estimation, data with global tilt removed. . . . .	64

## *List of Tables*

Table		Page
1.	Hartmann sensor subaperture centroid estimation test parameters: spot size and subaperture SNR. . . . .	33
2.	Four layer wind speed profile for fixed conditions prediction tests. Wind speeds are given per frame time. . . . .	43

*Abstract*

New methods for preprocessing wavefront sensor (WFS) slope measurements are presented. Methods are developed to improve the accuracy of WFS slope measurements, as well as estimating key atmospheric and system parameters from the slope signals. Both statistical and artificial neural network solutions are investigated. Also, new atmospheric models for generating slope and phase data with the proper spatial and temporal statistics are developed. The experiments in improving the accuracy of WFS slope measurements include reducing the WFS slope measurement error and compensating for adaptive optics system time delay through temporal slope prediction. The experiments in key parameter estimation include estimating the Fried coherence length,  $r_0$ , the wind speed profile, the strengths of the atmospheric turbulence layers, and the WFS mean square slope estimation error. Results of the experiments are used to make generalized conclusions in several key areas: first, the types of useful information that can be extracted from the WFS slope measurements; second, a comparison of linear or non-linear methods; and third, the possibility of methods that can be developed which operate over useful ranges of seeing conditions. Overall, we find that the WFS slope measurements do contain useful information which can be extracted through various techniques. Simple transformations (either by neural network or statistical solution) on slope measurements can yield significant improvements in system accuracy without major changes to the adaptive optics system. Also, we find that both neural networks and statistical methods perform well when seeing conditions are fixed, and that viable solutions can be developed that operate over broad ranges of seeing conditions. While developed to operate under variable seeing conditions, these solutions still provide significant performance in improving the accuracy of WFS slope measurements and in estimating key atmospheric and system parameters. In general, neural networks are much more robust when operating under variable seeing conditions than are the statistical solutions.

# LINEAR AND NON-LINEAR PREPROCESSING OF WAVEFRONT SENSOR SLOPE MEASUREMENTS FOR IMPROVED ADAPTIVE OPTICS PERFORMANCE

## *I. Introduction*

The resolution of ground based telescopes is limited by the random wavefront aberrations caused by atmospheric turbulence. Adaptive optics systems, which compensate for atmospheric effects, have been shown to improve the resolution of these telescopes. The purpose of an adaptive optics system is to remove the atmospheric induced aberrations from an incident optical wavefront. This is accomplished by measuring the incident aberrations and removing them using a deformable mirror. Correction with a deformable mirror must take into account the effects of additive noise in the wavefront sensor, system time delays, and the possibility of a spatial separation between the object of interest and the beacon used to measure the incident wavefront. The incident aberrations are measured with a wavefront sensor (WFS). A WFS, such as the Hartmann WFS, measures the localized slopes of the wavefront within subapertures of the telescope aperture. The deformable mirror then corrects for the measured aberrations based on a controlling algorithm. A controlling algorithm, or optimized reconstruction algorithm, translates WFS slope measurements into servo control commands for the deformable mirror, while trying to minimize the residual wavefront errors. However, there are several factors which limit the performance of adaptive optics systems. This chapter introduces some of the limiting factors that degrade adaptive optics performance as well as past solutions to adaptive optics problems. Also, new solutions to adaptive optics problems investigated in this research are described, along with the overall research goals and objectives.

### *1.1 Limits on Adaptive Optics Performance*

While adaptive optics have improved the performance of ground based telescopes, there are several factors which limit the performance of adaptive optics systems. The accuracy of the WFS is limited by camera read noise, shot noise, and the finite number of sampling areas across the optics diameter. Also, the ability of the deformable mirror to correct aberrations is limited by the finite number of degrees of freedom within the device. Since the wavefront aberrations evolve with time, the system time delay results in further system error. Finally, an optimal wavefront reconstruction algorithm, such as the minimum variance reconstructor, can be derived based on statistical knowledge of the atmosphere, noise and other random effects in the adaptive optics system. However, the actual performance of this reconstructor may be limited by imperfect knowledge of several key parameters [25, 26, 27] associated with the atmosphere and system. The key atmospheric parameters include the Fried coherence length,  $r_0$  [4], the strength of the atmospheric turbulence layers, and the wind speed profile. A key adaptive optics system parameter is the WFS mean square slope measurement error. One source of information which has not been fully exploited to improve adaptive optics system performance is the statistical information contained in the WFS slope measurements. Due to the correlations which exist in the slope measurements, valuable information about these atmospheric and system parameters, the WFS measurement error, and the temporal evolution of the atmosphere is contained within them. The purpose of this research is to explore the possibilities for extracting information about these parameters from the WFS slope measurements, and to examine methods of effectively increasing WFS slope measurement accuracy. The ability to accurately estimate key parameters for use in optimal wavefront reconstruction algorithms can result in optimal wavefront correction and improved image quality. Also, the ability to improve the accuracy of WFS slope measurements before sending them to a wavefront reconstruction algorithm will result in improved system performance.

## 1.2 *Past Solutions*

Past research has focused on improving adaptive optics performance by using statistical based methods. Due to the high correlations which exist in the WFS slope measurements, this focus on statistics based methods makes sense. However, statistics based methods for improving adaptive optics performance require knowledge of key parameters to operate, and will not continue to operate in an optimal fashion under changing atmospheric conditions (often called seeing conditions). Interest has been growing in applying artificial neural networks to adaptive optics problems. Neural networks offer non-linear solutions to problems with the possibility of operating over a wide range of seeing conditions. While a comprehensive discussion of neural networks can be found in reference [15], a short, qualitative discussion of the neural networks used in this research follows. Artificial neural networks were developed to imitate the responses of biological neurons. A common model of a neuron is the perceptron. A perceptron consists of several input nodes fully connected to an associative node. The perceptron is able to learn by adjusting the weighted connections so that a given input produces a desired response [15, 19]. The type of neural network used throughout this research is the multilayer perceptron network. A multilayer perceptron is composed of layers of perceptrons. Given enough nodes and training data, a multilayer perceptron network is capable of approximating any continuous, nonlinear function [15]. The networks used in this research consist of an input layer, a nonlinear hyperbolic tangent hidden layer, and linear summation output layer. The neural nets are trained using standard backpropagation techniques [14]. Training a neural network consists of propagating a large number of data vectors through the network one at a time. The output of the network is then compared to a desired output and the error is used to adjust the weighting of the connections between layers. The entire set of training data is repeatedly propagated through the network until the network converges on a solution which minimizes the total error over the entire training data set. Once the network has converged on a solution, the weights are fixed and the network is tested with an independent set of data vectors. When

results are mentioned in this paper, they reflect the performance of a neural network on the test data and not the training data.

Very little work has been done in the area of applications of neural networks to adaptive optics systems. Previous work has been performed in the area of using neural networks to replace the function of traditional wavefront sensors (such as the Hartmann wavefront sensor) [2, 11, 12, 30]. Specifically, this previous work dealt with using an in and out of focus image of a guide star as the input vectors to a neural network. The network was then trained to provide estimates of the low order Zernike components of the wavefront. The results obtained from these networks were comparable to those obtained using a traditional wavefront sensor. Recently, work has been reported which used neural networks to predict future wavefront measurements [6, 7, 8, 9]. This work began by predicting overall wavefront piston and tilt, but eventually evolved to predicting the  $x$ -components of the slope for the individual wavefront elements. While good performance was achieved, the network had to be trained for a specific set of conditions. Therefore, if conditions changed, a new set of network weights would be required. Past research efforts in adaptive optics have shown that improvements in performance can be reached. The question left unanswered is if solutions can be found which will operate when the seeing conditions are changing.

### *1.3 Improving WFS Slope Measurement Accuracy*

A large source of error in today's adaptive optics system lies in the accuracy of the WFS slope measurements. If the WFS slope measurements do not accurately represent the true subaperture slopes at the time of wavefront correction a performance degradation occurs. There are two major sources of inaccuracy in the WFS slope measurements. They are the WFS slope measurement error, and the system time delay. This section outlines approaches for improving the accuracy of the WFS slope measurements in each of these areas.

*1.3.1 WFS Slope Measurement Error.* Reduction of the WFS slope measurement error is one area of particular interest to users of adaptive optics systems. The error introduced into the wavefront measurements by the wavefront sensor is random. This error arises from such sources as charge-coupled device (CCD) read noise and shot noise. Since the goal of adaptive optics is to correct for the atmospheric aberrations as measured by a WFS, reducing the WFS measurement error would be of great benefit to adaptive optics system performance. Methods of reducing WFS measurement error investigated in this research include processing of the entire set of WFS slope measurements at once, and improving the measurement accuracy within a single WFS subaperture by processing the raw detected optical signal.

*1.3.1.1 Processing an Entire Set of WFS Slope Measurements.* In the case of processing a single frame of WFS slope measurements, if one can learn the current statistics of the slope signals and additive noise either through mathematical calculations or by training a neural network, then the information could be used to reduce noise effects. It can be shown that with knowledge of the wavefront slope signal statistics, a simple linear transformation of WFS measurements can reduce the variance of the error [20]. The WFS measurement error can be viewed as noise, with the true slope value being the signal. In the case where the signal and noise are independent and both follow normal distributions (assumptions commonly made in adaptive optics) [24], a linear transformation can be produced which yields the Bayes optimal estimate of the signal based on a noisy, or erroneous measurement. If the measured signal is viewed as a vector  $\vec{x}$  of measurements, where

$$\vec{x} = \vec{s} + \vec{n} \quad (1)$$

and  $\vec{s}$  is the true slope measurements and  $\vec{n}$  is the measurement error, then our estimate of the error free slope measurements,  $\hat{\vec{s}}$ , is

$$\hat{\vec{s}} = P\vec{x}. \quad (2)$$

The matrix  $P$  is the Bayes optimal error reducer, a linear transformation where

$$P = R_s[R_s + R_n]^{-1} \quad (3)$$

and  $R_s$  is the signal covariance matrix and  $R_n$  is the noise covariance matrix.

Except for the case where no error is present, a linear transformation via the matrix  $P$  is guaranteed to reduce the variance of the measurement error in the slope measurement. In the case of no noise, the matrix  $P$  becomes the identity matrix and no change to the measured signal occurs. This Bayes optimal linear transformation represents the best mean square slope estimation error reduction possible given the assumptions on the distributions of the data. However, implementing such a transformation may not always be possible. Prior knowledge of the signal and noise covariances is required to produce the matrix  $P$ . In real world applications, conditions, and thus the covariances, are continually changing. Therefore, knowing which values of signal and noise covariance to use at any given time is problematic. Neural networks, which can be trained to operate over a wide range of conditions, offer the possibility of taking advantage of the covariances and correlations between wavefront measurements to implement a mean square slope measurement error reduction scheme. While the best performance that a neural network can be hoped to achieve is equal the optimal statistics based solution, a network should be able to perform error reduction without the need to know the current statistics of the signal and noise. Previous research has shown that neural networks can be used to reduce the noise in measured signals [21, 31]. Again, since the WFS measurement error can be modeled as noise, noise reduction techniques should apply to reducing the WFS slope estimation error.

*1.3.1.2 Reducing Error Within a Single Subaperture.* In the case of improving measurement accuracy within a single WFS subaperture, we must understand the source of the errors better. In a Hartmann WFS, one of the most common WFSs in use with adaptive optics, a point source is imaged through subapertures of the telescope aperture onto detector arrays. The location of the centroid of the image formed on the detector

array is directly related to the localized slope of the incident wavefront within the given subaperture. The main source of error in the Hartmann sensor is that the main lobe of the irradiance pattern produced on the detector array may be smaller than the physical dimensions of the detector array elements. When the main lobe of the image is smaller than a single detector array element, one of two results may occur. When the main lobe falls on several detectors as in Point A of Fig. 1, then centroid estimation can be very accurate. However, as the main lobe of the image moves across a single detector as in Point B of Fig. 1, it is quite obvious which detector contains the image centroid, but exactly where it lies within the individual detector is not certain. Because the energy falling on the detectors other than the one containing the centroid is very small, the read and shot noise in these detectors corrupt the detected signal, making it difficult to use the energy outside the main lobe to pinpoint the centroid location. Thus, as the image centroid moves across a single detector, it is very hard to estimate its exact location. The other source of error is the presence of read and shot noise in the detectors. These random effects distort the detected image and thus can effect the estimated centroid location. Overall, errors in the slope measurements result in imperfect wavefront compensation by the deformable mirror.

Many adaptive optics systems use a quad-cell, or a  $2 \times 2$  array of detectors for centroid estimation within a subaperture. However, there has been a move to use larger arrays of detectors per subaperture for one of two reasons. One reason is to improve the dynamic range of slope estimation, the other is to improve the resolution in centroid estimation. In either case, the increase in detector array size makes the effects of read noise more significant. In this research we choose to investigate estimating the centroid location within a WFS subaperture for  $4 \times 4$  detector arrays. Both read noise and shot noise are factored into data generation. A standard centroid estimation algorithm exists, but as the number of detectors increases, the slope measurements errors due to noise effects increase. Because neural networks can be trained with noisy data, and thus learn to operate well in noisy conditions, they make excellent candidates for improving centroid location estimation within

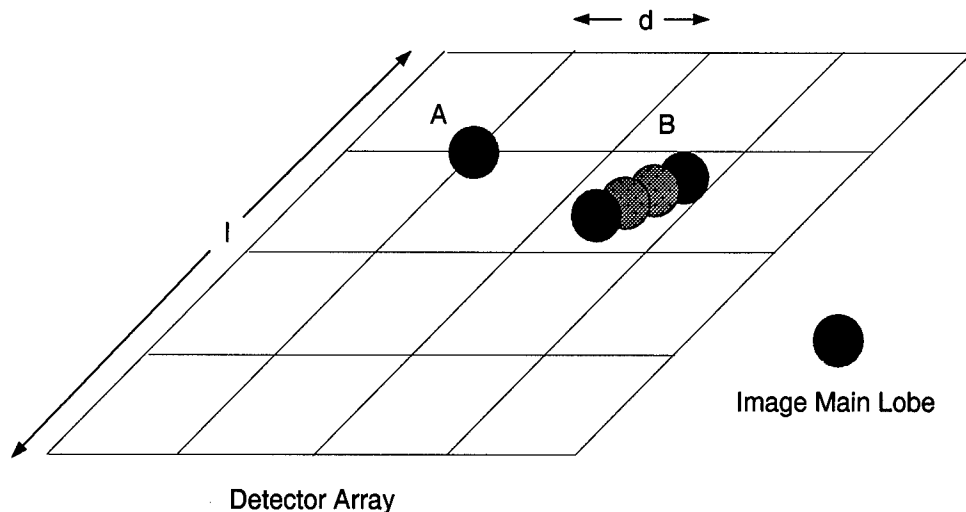


Figure 1. Lenslet image on detector array when image main lobe is smaller than a single detector.

a Hartmann WFS subaperture. Therefore, in this research artificial neural networks are trained to take as input the detected signal from each detector within a subaperture and estimate both the  $x$  and  $y$  centroid locations. The results obtained using the neural networks are then compared to a standard centroid estimation algorithm for noise free data, as well as with data which take into account both read and shot noise. In the tests which take into account noise effects, noise conditions consistent with both natural guide stars and artificial beacons are considered. Tests are conducted on lenslets where the main lobe of the speckle image is both a full, and half of a detector pixel's width.

*1.3.2 System Time Delay.* Another source of wavefront reconstruction error which is of interest is the system time delay. While it would be impossible to build an adaptive optical system without delay, it may be possible to predict the wavefront at the time of wavefront compensation based on past measured slopes. A statistical technique exists for slope prediction which relies on knowledge of the key atmospheric and system parameters. This technique is based on knowing the covariance of the measured WFS data. Artificial neural networks, which do not require knowledge of the key parameters or the

covariance statistics of the data, are compared to the statistical techniques. When seeing conditions are set, and thus the statistics of the slope measurements are fixed, a simple linear transformation can be used to perform prediction [10]. If we were to predict slope measurements at the time of wavefront compensation based on the previous two frames of measured slopes, then this linear transformation becomes

$$\hat{x}_t = \begin{bmatrix} A_1 & A_2 \end{bmatrix} \begin{bmatrix} x_{t-1} \\ x_{t-2} \end{bmatrix}, \quad (4)$$

where  $\hat{x}_t$  is the vector of estimated slopes at time  $t$ , and  $x_{t-1}$  and  $x_{t-2}$  are two previous vector frames of noisy slope measurements. The matrices  $A_1$  and  $A_2$  are found by solving [10]

$$\begin{bmatrix} R_{xx}(0) & R_{xx}(-1) \\ R_{xx}(1) & R_{xx}(0) \end{bmatrix} \begin{bmatrix} A_1^T \\ A_2^T \end{bmatrix} = \begin{bmatrix} R_{xx}(1) \\ R_{xx}(2) \end{bmatrix}, \quad (5)$$

where  $R_{xx}(\hat{t})$  is the covariance matrix between two measurement frames separated by time  $\hat{t}$ .

This linear transformation is Bayes optimized in the mean square sense for data governed by Gaussian point statistics, and thus represents the best prediction possible for WFS slope data when the statistics of the signal are known. However, implementing such a transformation may not always be possible. Prior knowledge of the signal and noise covariances are required to produce the matrix  $R_{xx}(\hat{t})$ . In real world applications, conditions are continually changing and thus these covariances are continually changing. Therefore, knowing which values of signal and noise covariance to use at any given time is a difficult task. Neural networks, which can be trained to operate over a wide range of conditions, offer the possibility of taking advantage of the covariances and correlations between wavefront measurements to implement a prediction scheme. While the best performance that a neural network can obtain is to equal the Bayes optimal solution given above, a network should be able to perform prediction without the need to know the current statistics of the signal

and noise. Also, because anisoplanatism, or a spatial separation between the beacon and the object of interest, can be modeled as a temporal prediction problem where the wind speeds are fixed [18], any results obtained from the tests in prediction will apply to the problem of anisoplanatism.

#### 1.4 Key Parameter Estimation

Parameter estimation is another application investigated in this research. Neural networks and statistical methods may be able to predict key atmospheric parameters such as the Fried coherence length,  $r_0$ , the relative strengths of the atmospheric layers, and the wind speed profile, as well as key system parameters such as the WFS mean square measurement error. Knowledge of the current state of these parameters would enable better wave front reconstruction using statistical based optimal reconstructors. Because the covariance properties of the WFS slope measurements are directly related to these key parameters, a neural network or statistical method may be able to operate on slope measurements to estimate the current value of these parameters. Statistics based wavefront reconstruction algorithms, such as the minimum variance reconstructor, compensate for system time delay, reduce wavefront sensor measurement error, and compensate for separation between a guide star and the object of interest. These techniques are optimized to reduce the variance of the residual phase errors after correcting an aberrated wavefront with a deformable mirror [3, 24, 25, 26, 27]. These statistics based reconstruction algorithms have also been shown to produce better wavefront reconstruction than least squares techniques [17]. However, the “optimality” of these algorithms is heavily dependent on knowing the current state of such parameters as  $r_0$ , the relative strengths of the atmospheric layers, the wind speed profile, and the WFS measurement error. The problem is in maintaining a good estimate of these parameters as the atmosphere evolves over time. This research investigates using neural networks and statistical methods to estimate these key parameters in order to improve the “optimality” of statistics based reconstruction algorithms.

### 1.5 *Research Goals and Overview*

While improving the accuracy of WFS slope measurements and key parameter estimation are both key issues in the adaptive optics community, processing of the WFS slope measurements to perform these tasks has not been previously investigated. Because the key parameters of  $r_0$ , the atmospheric layer strengths measured as the fraction of all turbulence in each atmospheric layer, the wind speed profile, and the WFS mean square slope estimation error all contribute to the statistics of the measured atmospheric aberrations, it may be possible to estimate them from the WFS slope measurements. Also, due to the high degree of both spatial and temporal correlation within the slope measurements, direct processing of the slope measurements should yield better estimates of the true slopes at the time of wavefront compensation. The ability to have real-time estimates of key parameters along with improving the WFS estimated slope signal accuracy are crucial to improving adaptive optics performance. Therefore, individual experiments in key parameter estimation and improving the accuracy of WFS slope measurements make up the heart of this research. However, the main focus of this research is to make broad conclusions from the individual experiments on the following key issues:

1. What kinds of useful information can be extracted from the WFS slope measurements?
2. Which methods work best (linear/statistical methods or non-linear methods/artificial neural networks)?
3. Can methods be developed which operate over useful ranges of seeing conditions?

The first issue deals with what can we reasonably expect to extract from the WFS slope measurements. As was stated earlier, many factors effect the statistics which ultimately govern the atmospheric aberrations and the limits on adaptive optics system performance. To understand what information can be gained by preprocessing WFS slope measurements, we investigate whether the following tasks can be accomplished:

- improving the WFS estimated slope signal

- reduction of the WFS mean square slope estimation error
- slope prediction to compensate for system time delay
- key parameter estimation
  - estimation of the parameter  $r_0$
  - estimation of the relative strengths of the atmospheric layers
  - estimation of the atmospheric wind speed profile
  - estimation of the WFS mean square slope measurement error

The second issue deals with choosing the proper method for extracting information from WFS slope measurements. This research compares the performance of linear (statistics based) methods with non-linear methods (artificial neural networks). We must understand the benefits and limitations of neural networks as compared to statistics based methods. This research applies both linear and non-linear methods to each of the tasks listed above. The results of each are compared to understand several issues. The first is the ability of a neural network to approximate the optimal statistical solution when seeing conditions are fixed. Many of the statistical methods available for performing the tests require knowledge of the key parameters not being estimated. Perfect knowledge of these other parameters results in an optimized statistical solution to the problem. While it has been shown in theory that neural networks should approximate these optimized solutions [28], it has not been shown in practice that neural networks will approximate optimized statistical solutions to continuous function estimation processes. While comparisons of neural networks to optimized solutions sheds some light on the upper limit of performance, rarely in the real world do seeing conditions remain fixed. Therefore, experiments are also conducted with variable seeing conditions. The performance of neural networks is then compared to statistical solutions which have been fixed to some specific values of the key parameters which govern them. In the area of parameter estimation, the statistical estimators are optimized for averaging the estimate over many frames of slope measurements. Therefore, comparisons are made as to how many estimates must be averaged for both the neural

network and the statistical methods to achieve small errors. Finally, we must understand the effects of removing the global tilt across the aperture on both the statistical methods and the neural networks. Removing global tilt reduces the variance of the slope signals, and thus reduces the required dynamic range of the corrective optics. This reduction has the effect of making the individual slope measurements more independent of each other. While removing global tilt simplifies the adaptive optics system, we must understand what impact it has on the information contained in the WFS slope measurements. Therefore, tests are conducted on data with and without global tilt.

The final issue deals with developing flexible solutions to improving adaptive optics performance. When seeing conditions are fixed, highly accurate parameter estimation, noise reduction, and prediction can be accomplished through statistics based solutions. However, seeing conditions rarely remain fixed for any significant period of time. Therefore, any viable solution must be able to operate over a useful range of seeing conditions. Tests are conducted to determine not only how well the neural networks and statistical solutions perform under fixed conditions, but also how well a single, set neural network or statistical solution performs when the data is drawn from a variable range of seeing conditions.

Overall, we find that the WFS slope measurements do contain useful information that can be extracted through various techniques. From reducing WFS measurement error, to temporal slope prediction, to parameter estimation, significant performance increases can be realized either directly through processing of the WFS slope measurements, or by using parameter estimates from the WFS slope measurements to increase the performance of wavefront reconstruction algorithms. Also, we find that both neural networks and statistical methods perform well when seeing conditions are fixed, however neural networks are much more robust when operating under variable seeing conditions than are the statistical solutions. Finally, we find that viable solutions can be developed which operate over broad ranges of seeing conditions.

## *1.6 Dissertation Organization*

This dissertation is organized to first establish the foundation for the work, then provide the results of that work. Because all the data used for training and testing artificial neural networks are computer generated, Chapter II provides a detailed description of how the data are generated. Chapters III and IV discuss the tests and results in the areas of improving the accuracy of WFS slope measurements, and key parameter estimation respectively. Finally, Chapter V provides the overall conclusions.

## II. Data Generation

Before the tests mentioned in Chapter I can be conducted, a means of generating random data with the proper spatial and temporal statistics is required. Large sets of random data must be generated to train neural networks. Other data, independent of that used to train the networks, must also be generated to test the networks and the statistical models. These data must be governed by the proper spatial and temporal statistics. However, no model existed before this research for generating either slope or phase data with the proper spatial and temporal statistics. Therefore, the first step of this research is to develop the necessary models. If we can calculate the covariances between all of the data, then we can generate random draws of those measurements [16]. Therefore, expressions for the slope and phase covariances are developed. These expressions are based on turbulence statistics having a Kolmogorov power spectrum and the assumption that the atmosphere can be modeled as  $N$  independent turbulent layers, each with its own  $r_0$  and wind speed velocity. For this research, an atmosphere with four independent layers based on the Submarine Laser Communication night (SLC-N) profile is used [13, 22].

### 2.1 WFS Slope Measurement Data Generation

Tests in prediction, parameter estimation, and WFS measurement error reduction through processing of a single frame of WFS slope measurements, require random slope values with the proper spatial and temporal statistics. Starting with an equation developed by Ellerbroek [3], the following expression for the covariance,  $C_s$ , between any two zero mean, normally distributed slope measurements  $s_i(t_1)$  and  $s_j(t_2)$  at times  $t_1$  and  $t_2$  can be written (see derivation in Appendix A):

$$\begin{aligned}
C_s(s_i(t_1), s_j(t_2)) &= E[s_i(t_1)s_j(t_2)] \\
&= -3.44 \left(\frac{D}{r_0}\right)^{\frac{5}{3}} \sum_{k=1}^N f(z_k) \\
&\quad \times \int \int d\vec{x}_1 d\vec{x}_2 w_i^s(\vec{x}_1) w_j^s(\vec{x}_2) |\vec{x}_1 - \vec{x}_2 - (t_1 - t_2)\vec{v}(z_k)|^{\frac{5}{3}}.
\end{aligned} \tag{6}$$

The parameter  $D$  is the side length of the square system aperture (see Fig. 2),  $r_0$  is the Fried coherence length,  $f(z_k)$  is the fraction of overall turbulence in layer  $k$  at altitude  $z_k$ ,  $\vec{v}(z_k)$  is the wind velocity of layer  $k$ , and  $w_i^s(\vec{x})$  designates the gradient of the  $i$ th WFS subaperture weighting function which has different forms for  $x$  and  $y$  slope measurements. For square subapertures we have for an  $x$  slope measurement,

$$w_i^s(\vec{x}) = w_i^s(x, y) = \frac{1}{L_x L_y} \text{rect}\left(\frac{x - x_i}{L_x}, \frac{y - y_i}{L_y}\right) \left(\delta\left(x - x_i - \frac{L_x}{2}\right) - \delta\left(x - x_i + \frac{L_x}{2}\right)\right) \tag{7}$$

and for a  $y$  slope measurement,

$$w_i^s(\vec{x}) = w_i^s(x, y) = \frac{1}{L_x L_y} \text{rect}\left(\frac{x - x_i}{L_x}, \frac{y - y_i}{L_y}\right) \left(\delta\left(y - y_i - \frac{L_y}{2}\right) - \delta\left(y - y_i + \frac{L_y}{2}\right)\right), \tag{8}$$

where  $L_x$  and  $L_y$  are the  $x$  and  $y$  dimensions of the subaperture and  $(x_i, y_i)$  is the center location of the  $i$ th subaperture (see Fig. 2).

After using Eqn. (6) to compute the covariance matrix for an array of WFS subapertures, a method is developed for generating random draws of the slopes [16]. The slope covariance matrix calculated,  $C_s$ , is guaranteed to be symmetric, real, and positive definite, and therefore can be Cholesky factored into the product of two matrices such that:

$$C_s = RR^T. \tag{9}$$

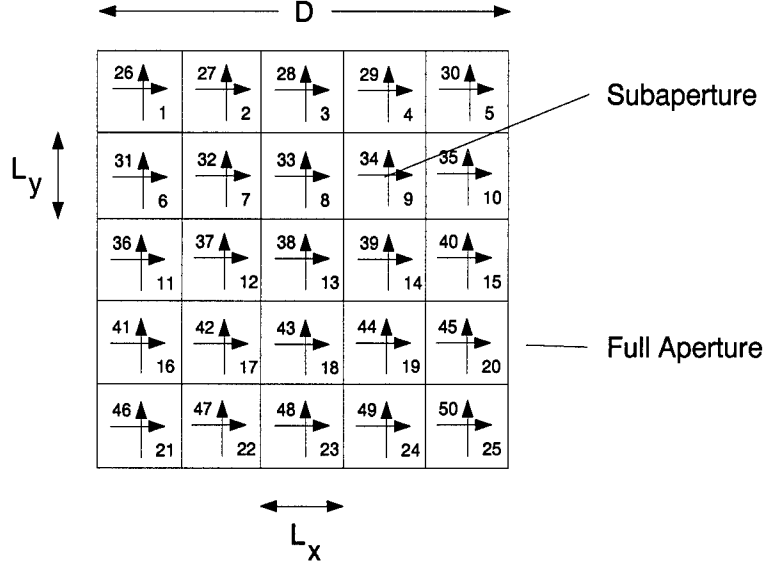


Figure 2. WFS subaperture geometry. Numbering depicts placement of each of the 50 slope measurements in the 50 element slope vector.

In order to generate series of random slopes with the proper space and time correlation properties, a zero mean, unit variance, white Gaussian random vector,  $\alpha$  is generated. These properties imply  $E[\alpha\alpha^T] = I$  where  $\alpha^T$  is the transpose of the vector  $\alpha$ , and  $I$  is the identity matrix. The vector  $\alpha$  is then multiplied by the matrix  $R$ . The resulting vector,  $R\alpha$ , represents the random slopes within each subaperture in space and time and exhibits the correct covariance as shown previously in reference [16]. For this research, the random slopes are generated for a  $5 \times 5$  array of subapertures, each with an  $x$  and  $y$  slope. Therefore, each realization of the slopes consists of 50 numbers (25  $x$  slopes and 25  $y$  slopes). Figure 2 depicts the geometry of the subapertures within the overall aperture.

Tests in parameter estimation and WFS measurement error reduction through processing a frame of WFS slope measurements require only individual frames of slope measurements. Therefore, the wind speeds of the atmospheric layers do not impact the data. However, before generating prediction data which is based on temporal sequences of data, we must set a limit on the maximum wind speed each layer may have in both the  $x$  and  $y$  directions. In an adaptive optics system which does not employ predictive techniques

(that is correction after the system time delay is based solely on the past measured slope values), wind speed conditions are limited by the correlation between a slope at the time of measurement and that same slope at the time of correction. Statistically, this implies that adaptive optics only improve image quality when the mean square difference of the current true slope measurement and the past noisy slope measurement is less than the mean square variation of the current true slope measurement:

$$E \{ (s_t - s_{t-\tau})^2 \} \leq E \{ s_t^2 \}, \quad (10)$$

where  $s_t$  represents the true slope at the time of wavefront correction and  $s_{t-\tau}$  is the past measured slope. Simplifying Eqn. (10) into the form of a correlation coefficient yields

$$\frac{E \{ s_t s_{t-\tau} \}}{\sqrt{E \{ s_t^2 \} E \{ s_{t-\tau}^2 \}}} \geq \frac{1}{2}. \quad (11)$$

Because  $s_t$  and  $s_{t-\tau}$  are both proportional to  $\frac{D}{r_0}$  (see Eqn. (6)), the left-hand side of Eqn. (11) is independent of  $\frac{D}{r_0}$ . However, it does depend on the number of subapertures in the wavefront sensor, the mean square slope estimation error of the subapertures, and on the magnitude of the wind speed profile. For this research, when we use a  $5 \times 5$  array of subapertures, global tilt removed data, and a worst case slope measurement error of 25% of the slope variance, it is empirically determined that Eqn. (11) is satisfied when the maximum velocity each layer can have is  $0.1D$  per frame. That is if all four layers have both  $x$  and  $y$  velocities exceeding  $0.1D$  per frame, then the system time delay would be sufficiently large that correction using adaptive optics would hurt performance rather than improve it. Therefore, for this research, wind speeds are limited to a maximum of  $0.1D$  per frame. This allows comparison of the prediction techniques to the performance of an adaptive optics system which does not implement predictive techniques.

## 2.2 Phase Screen Data Generation

Tests in reducing the WFS slope measurement error within a single WFS subaperture require phase screen data with the proper spatial statistics. Starting with an equation developed by Ellerbroek [3], the following expression for the covariance,  $C_p$ , between the phase at any two locations within the subaperture,  $\vec{x}_1$  and  $\vec{x}_2$ , assuming the phase measurements are zero mean and normally distributed, can be written (see derivation in Appendix B):

$$\begin{aligned}
 C_p(\vec{x}_1, \vec{x}_2) &= E[\phi(\vec{x}_1)\phi(\vec{x}_2)] \\
 &= -3.44 \left(\frac{L}{r_0}\right)^{\frac{5}{3}} \left[ W(\vec{\eta})W(\vec{\xi}) (|\vec{x}_1 - \vec{x}_2|)^{\frac{5}{3}} - \int d\vec{\xi} W(\vec{x}_1)W(\vec{\xi}) (|\vec{x}_1 - \vec{\xi}|)^{\frac{5}{3}} \right. \\
 &\quad \left. - \int d\vec{\eta} W(\vec{\eta})W(\vec{x}_2) (|\vec{\eta} - \vec{x}_2|)^{\frac{5}{3}} + \int \int d\vec{\phi} d\vec{\theta} W(\vec{\phi})W(\vec{\theta}) (|\vec{\phi} - \vec{\theta}|)^{\frac{5}{3}} \right],
 \end{aligned}
 \tag{12}$$

$$\tag{13}$$

where  $\phi(\vec{x}_i)$  is the phase at location  $x_i$ ,  $L$  is the dimension of the lenslet aperture,  $r_0$  is the Fried coherence length, and  $W(\vec{\alpha})$  is the lenslet aperture function with values of 1 inside the aperture and 0 outside the aperture. Equation (13) can be easily solved for any two points using Gegenbauer polynomials [23] (see Appendix C).

After using Eqn. (13) to compute the phase covariance matrix for an array of points within a subaperture, the method for generating random draws of the slopes [16] is again used for phases. Because the phase covariance matrix,  $C_p$ , is guaranteed to be symmetric, real, and positive definite, we can Cholesky factor it into the product of two matrices such that:

$$C_p = RR^T. \tag{14}$$

In order to generate random phases screens with the proper spatial correlation properties, a zero mean, unit variance, white Gaussian random vector,  $\alpha$  is generated. These properties imply  $E[\alpha\alpha^T] = I$  where  $I$  is the identity matrix. The vector  $\alpha$  is then multiplied by the matrix  $R$ . The resulting vector,  $R\alpha$ , represents the random phases within the subaperture

and exhibits the correct covariance. For this research, the random phases are generated for a  $41 \times 41$  array of points.

Once the phase screens are generated, the image of a point source within the WFS subaperture is simulated and superimposed on a  $4 \times 4$  detector array. In order to model read and shot noise under realistic conditions, an expression is developed for the signal to noise ratio (SNR) at the detector array. The expression for the SNR (as derived in Appendix D) is

$$\text{SNR} = \frac{K}{\sqrt{0.0346K + 2.5\sigma_e^2}}, \quad (15)$$

when the main lobe of the image is half the width of a detector, and

$$\text{SNR} = \frac{K}{\sqrt{0.0378K + 2.5\sigma_e^2}}, \quad (16)$$

when the main lobe of the image is the full width of a detector. In these expressions,  $K$  is the average count detected per measurement per subaperture, and  $\sigma_e$  is the root mean square read noise count of a single detector element. While this expression does not represent a SNR in the traditional sense, it is widely used in the adaptive optics community. With this expression in mind, appropriate ranges of SNR must be determined to represent both natural guide stars and artificial beacons. We find that a typical natural guide star provides a SNR between 4.0 and 7.5 (low SNR case), while a typical artificial beacon provides a SNR between 7.5 and 11.0 (high SNR case). These SNR ranges are based on  $\sigma_e = 12$  electrons and  $K = 100$  photo events per lenslet for a natural guide star and 180 photo events per lenslet for an artificial beacon [1]. To keep this work independent of the system specifications, a SNR is randomly chosen in the proper range for each simulated image. The photo electron generation rate,  $K$ , is kept constant at 150 photo events per lenslet, and the value of the read noise,  $\sigma_e$ , is calculated using either Eqn. (15) or Eqn. (16). Detector shot noise is modeled as a Poisson random variable with arrival rate dependent on  $K$ , and detector read noise is modeled as an additive, independent, Gaussian random variable with variance  $\sigma_e^2$ .

To properly account for noise, the percent of the subaperture irradiance on each detector pixel in the array is determined. This percentage of  $K$  is the assumed average count detected for that pixel, and is used as the arrival rate for a Poisson number generator. Then read noise with the appropriate variance is added to each detector pixel. Once noise is accounted for, a signal count for each detector in the array is calculated for each data image. The detector counts for each image are then normalized by the largest detector value for that image. This makes the data independent of the value chosen for  $K$ , and thus all neural network solutions derived are dependent only on the SNR of the data.

Once methods exist for generating random slope and phase screens with the proper spatial and temporal statistics, the large sets of data to train and test artificial neural networks and to test the statistical methods can be generated. With the ability to generate both slope and phase screens, the data requirements of all the tests conducted in this research are met.

### *III. Improving the WFS Estimated Slope Signal*

One key to improving the performance of adaptive optics systems is in improving the WFS estimated slope signals. Improvements can be made in terms of reducing the WFS mean square slope estimation error, predicting the slope measurements at the time of correction with the deformable mirror, or compensating for anisoplanatic effects. The ability to make these improvements on the raw slope measurements before feeding them to the wavefront reconstruction algorithm would reduce the burden on the reconstruction algorithm of performing many tasks at once. Improving the accuracy of the WFS slope measurements should yield improved adaptive optics performance, while also allowing the possibility of less complex reconstruction algorithms.

#### *3.1 Reduction of WFS Slope Measurement Error*

One key area to improving adaptive optics performance is the area of reducing the WFS mean square slope measurement error. Again, since adaptive optics systems correct wavefront phase variations based on the WFS slope measurements, the less error in estimating the slopes, the better the wave front reconstruction. This research investigates two methods by which WFS slope measurement error can be reduced. The first involves processing an entire frame of WFS slope measurements at once, and using the covariance statistics of the slope measurements to reduce the measurement error. The second method involves improving the measurement accuracy within an individual WFS subaperture.

##### *3.1.1 Reduction of WFS Slope Measurement Error Through Slope Vector Processing.*

The goal of this portion of the research is to take slope measurements with measurement error, and try to reduce the WFS error level. As was stated earlier, and shown in Eqn. (3), a Bayes optimal solution exists for measurement error reduction, but it requires knowledge of the signal and error covariance matrices. We compare neural network performance to the performance of this optimal solution. In order to understand the performance of

both statistical and neural network solutions for WFS measurement error reduction, two experiments are conducted. The first experiment deals with fixed conditions. That is, the free parameters which ultimately define the statistics of the WFS measurements are not allowed to vary. These parameters are  $D/r_0$  and the slope measurement error level. This experiment shows how well a neural network can approximate the Bayes optimal solution. However, in real applications, these parameters are continually changing with time, and their values at any instant in time are not known. Therefore, for either solution to be viable, it must operate over a broad range of these parameters. In the second experiment, these parameters are allowed to vary.

In the first experiment, two tests are conducted to determine how well a neural network approaches the Bayes optimal solution for fixed conditions. These tests include low and high measurement error cases. For both tests, a  $5 \times 5$  array of subapertures is used and random slopes are generated with  $D/r_0 = 1$ . With  $D/r_0 = 1$ , the variance of the individual slope elements, as calculated in Eqn. (6), is  $0.43\text{rad}^2/\text{m}^2$ . In the low measurement error case, independent Gaussian noise with a variance of  $0.043\text{rad}^2/\text{m}^2$  is added to each slope measurement, yielding a SNR of 10. For the high measurement error case, noise with a variance of  $1.00\text{rad}^2/\text{m}^2$  is added, yielding a SNR less than 1/2. In both cases, a neural network with 60 hidden layer nodes and 50 linear summation output nodes is trained to perform measurement error reduction. The neural network is trained to take a single, 50 element, WFS measurement as input, and estimate the true, 50 element WFS slope vector as output. The Bayes optimal solution operates in the same manner. Vectors of the WFS measurements are matrix multiplied with Eqn. (3) with the result being an estimate of the true WFS data. For both methods, the MSE between the estimated and true WFS data for each element of the slope vector is calculated over 10000 randomly generated slope vectors using

$$\epsilon_i^2 = \frac{1}{10000} \sum_{j=1}^{10000} (\hat{v}_{i,j} - v_{i,j})^2, \quad (17)$$

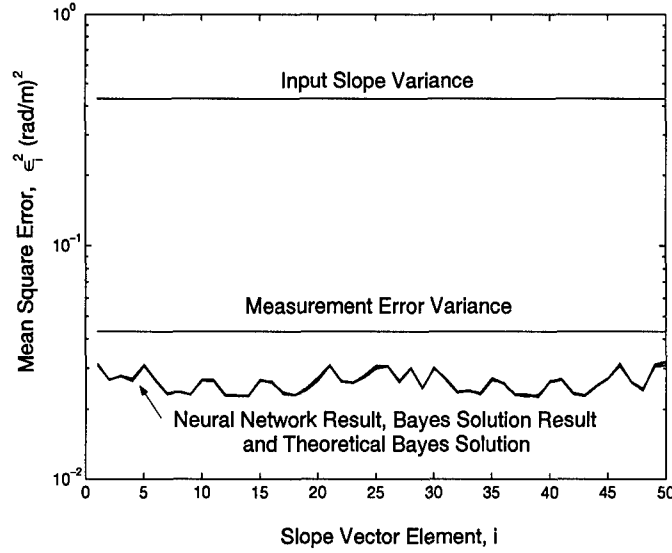


Figure 3. WFS slope measurement error reduction, low measurement error case (SNR = 10.0). MSE,  $\epsilon_i^2$ , plotted as a function of WFS slope index  $i$  (see Fig. 2). Parameters fixed at  $D/r_0 = 1.0$ , yielding a signal variance of  $0.43\text{rad}^2/\text{m}^2$ , and noise variance set at  $0.043\text{rad}^2/\text{m}^2$ .

where  $\hat{v}_{i,j}$  is the estimate of the  $i$ th slope element of the  $j$ th slope vector, and  $v_{i,j}$  is the true value of the  $i$ th slope element of the  $j$ th slope vector. Figure 3 shows the results for the low error level case, and Fig. 4 shows the results for the high error level case. The graphs are plots of the MSE as a function of the index of the 50 WFS slopes (see Fig. 2). Each graph shows the results of the neural network and the Bayes optimal solution on a common test set. Also shown is the theoretical result for the Bayes estimator, had a test set of infinite size been used. As can be seen by both graphs, the neural network is able to closely approximate the Bayes optimal solution. It can also be seen in Fig. 3 and Fig. 4 that the amount of error variance reduction is not constant across all 50 slopes. As expected, the slopes with the greatest amount of error reduction correspond to the slopes from the center subapertures in the  $5 \times 5$  WFS array, while slopes with the least amount of error reduction correspond to slopes from the edge and corner subapertures.

This first experiment shows that a neural network can approximate the Bayes solution for error reduction when the atmospheric and error conditions are fixed. However, in order

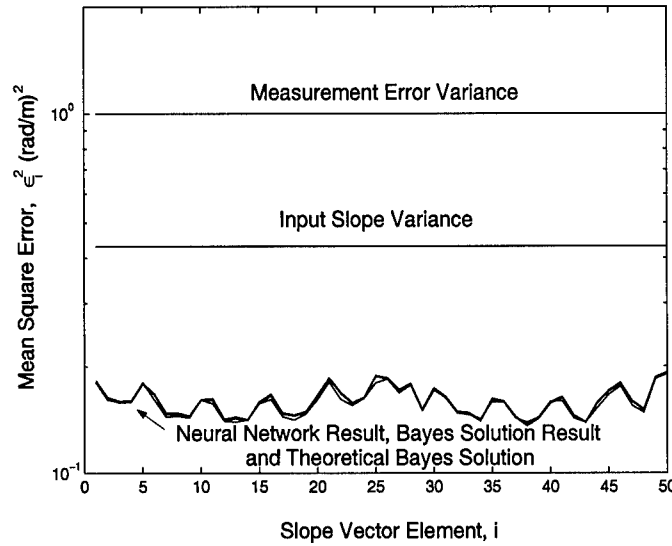


Figure 4. WFS slope measurement error reduction, high measurement error case (SNR = 0.43). MSE,  $\epsilon_i^2$ , plotted as a function of WFS slope index  $i$  (see Fig. 2). Parameters fixed at  $D/r_0 = 1.0$ , yielding a signal variance of  $0.43\text{rad}^2/\text{m}^2$ , and noise variance set at  $1.00\text{rad}^2/\text{m}^2$ .

to understand the issue of flexibility, an experiment is conducted over a range of conditions. For this test, a  $5 \times 5$  array of subapertures is again used.  $D/r_0$  is allowed to range between 5 and 10, or between 1 and 2  $r_0$ 's per subaperture. The additive measurement error level is randomly selected in the range of 0-25%, yielding a SNR of 4 and greater. A single neural network with 200 hidden nodes and a linear summation output layer of 50 nodes is trained to operate over the entire range of the data. The network inputs are the 50 WFS measurements, and the output is again an estimate of the actual slopes. The results achieved with the neural network are then compared to the true optimized Bayes solution for each individual set of 50 WFS measurements, representing the optimum error reduction possible for each individual set of 50 WFS slope measurements. For the comparison, sets of test data are generated at  $D/r_0$  values of 5.0, 7.5, and 10.0. Additive error is incremented by 5% steps from 0% to 25%. Figure 5 shows the results of these tests. Each graph is for a different  $D/r_0$  value and plots the average MSE versus percent measurement error. MSE,  $\epsilon^2$ , is as defined in Eqn. (17), except the MSE is averaged over all 50 elements of each slope

vector.

$$\epsilon^2 = \frac{1}{50} \sum_{j=1}^{50} \epsilon_j^2, \quad (18)$$

The lines on the graphs represent the results of the neural network and the optimized Bayes solution. The Bayes solution is considered optimized because it is based on perfect knowledge of  $D/r_0$  and the noise level for each test frame. Also shown is the variance of the original measurement error, or the amount of error that would be measured if neither method of noise reduction is used. These tests show that the neural network is able to do a significant amount of measurement error reduction over the entire range of error levels, although the optimized Bayes solution does better. The advantage is that the neural network does not require knowledge of the signal or measurement error statistics.

The question left unanswered is how dependent on  $D/r_0$  and the measurement error variance is the Bayes optimal solution. If the variance of the measurement error is defined as a fraction of the signal variance, the Bayes optimal solution is not dependent on  $D/r_0$  (in this case,  $D/r_0$  can be factored out of Eqn. (3)). Therefore, to test the flexibility of the Bayes solution, a single Bayes solution based on a measurement error variance of 12.5% (median value of the test data) is tested versus the neural network. We refer to this Bayes solution as the “suboptimized” solution since it is based on a single error level (12.5%) instead of the individual error levels of each frame. The results are shown in Fig. 6 for the case of  $D/r_0 = 10.0$ . Since the results for the Bayes solution are independent of  $D/r_0$ , this graph is representative of the solution for the full range of  $D/r_0$ . It should be noted that the suboptimized Bayes solution produces a straight line result that is tangent to the optimized solution curves shown in Fig. 5. The point of tangency coincides with the error level for which the suboptimized Bayes solution is matched. The suboptimized Bayes solution outperforms the neural network over the whole range of error variances. While this means that the suboptimized Bayes solution is the better method of error reduction, it also raises a new question regarding the use of neural networks in adaptive optics. Specifically, if neural networks can estimate the WFS measurement error level as a percent of the

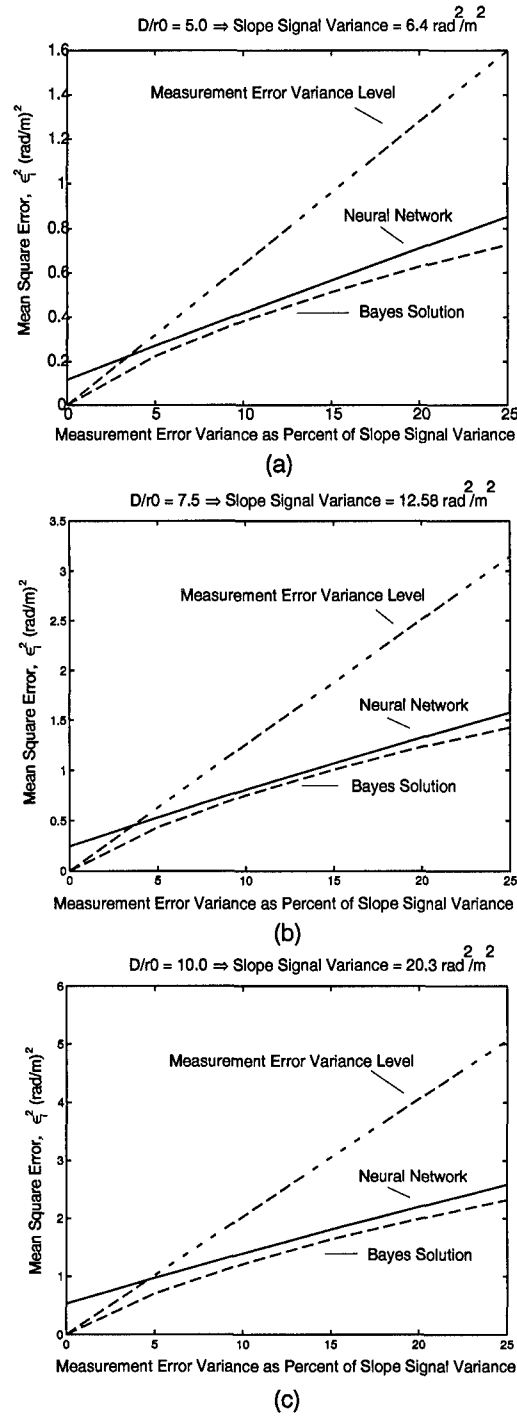


Figure 5. Comparison of neural network to Bayes optimal solution for WFS slope measurement error reduction. Average WFS slope MSE plotted versus measurement error variance for a)  $D/r_0 = 5.0$ , b)  $D/r_0 = 7.5$ , and c)  $D/r_0 = 10.0$ .

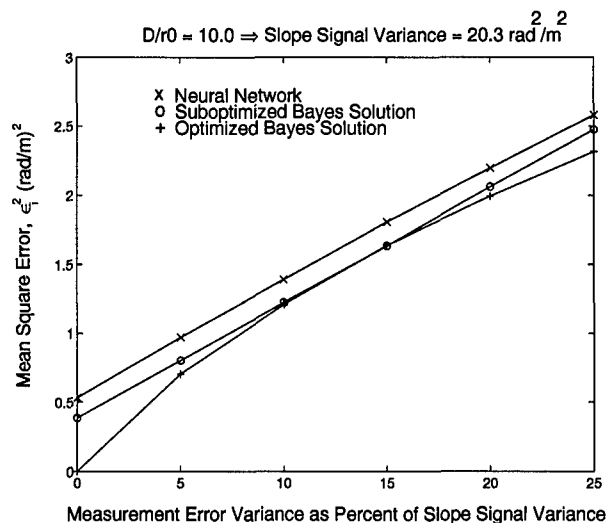


Figure 6. Comparison of neural network, optimized Bayes solution, and suboptimized Bayes solution (optimized for WFS slope measurement error 12.5%) for WFS slope measurement error reduction. Average WFS slope MSE plotted versus measurement error variance for  $D/r_0 = 10.0$ .

signal variance, then an optimized Bayes solution can be implemented. This question is addressed in the next section. To further understand how the neural network solution compares to the suboptimized Bayes solution over the entire range of  $D/r_0$  see Fig. 7. Both methods are tested on a common set of data for  $D/r_0$  ranging over 5 to 10. The results are shown for each individual element in the 50 elements slope vector. The upper line is the average measurement error level for the whole range of  $D/r_0$  values and error levels. The other lines represent the MSE after error reduction using either the neural network or the suboptimized Bayes solution (optimized for WFS slope measurement error level equal to 12.5%). While the suboptimized Bayes solution outperforms the neural network solution by a nearly constant factor, the neural network solution does match the shape of the suboptimized Bayes solution (see Fig. 7) while approximating the amount of error reduction.

To understand the effects of global tilt removal on measurement error reduction, a neural network with 220 hidden nodes is trained to perform error reduction on global tilt

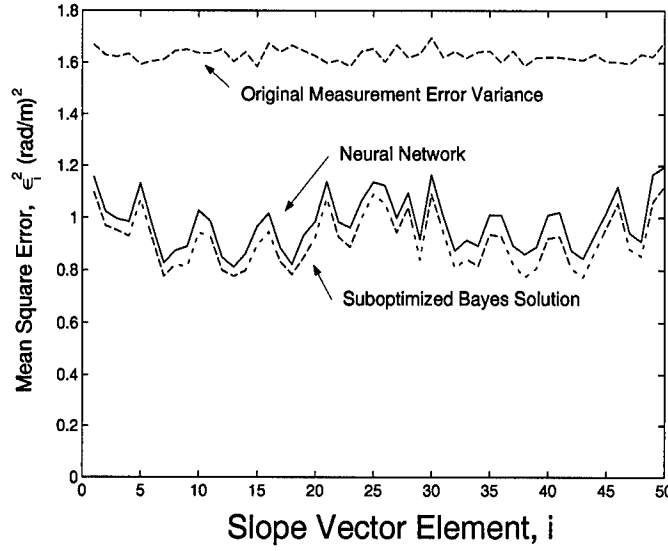


Figure 7. Average WFS slope mean square error plotted as a function of the slope measurement index (see Fig. 2) for  $D/r_0$  ranging between 5 and 10, and the WFS slope measurement error levels ranging between 0 and 25%. The three curves represent the original WFS slope measurement error level, the slope measurement error level after neural network processing, and the slope measurement error level after processing with a suboptimized Bayes solution (optimized for  $D/r_0 = 7.5$  and WFS slope measurement error level 12.5%).

removed data with  $D/r_0$  in a range of 5-10, and measurement error level in the range of 0-25%. The performance of the network is then compared to both an optimized and suboptimized Bayes solution. The suboptimized Bayes solution is again set for a measurement error level of 12.5%. As stated before, removing global tilt from the data reduces the variance of the individual slope measurements and makes them more independent. This reduction in the relative magnitude of the off diagonal elements of the slope covariance matrix can be seen in Fig. 8. Since error reduction, especially the Bayes solution, is dependent on the relationships or covariances between measurements, we would expect the amount of error reduction to be less for global tilt removed data than for data with global tilt included. This decrease in the amount of relative error reduction can be seen in Fig. 9, where the neural network is compared to the optimized Bayes solution. This same decrease in the amount of relative error reduction can also be seen in Fig. 10, where the network

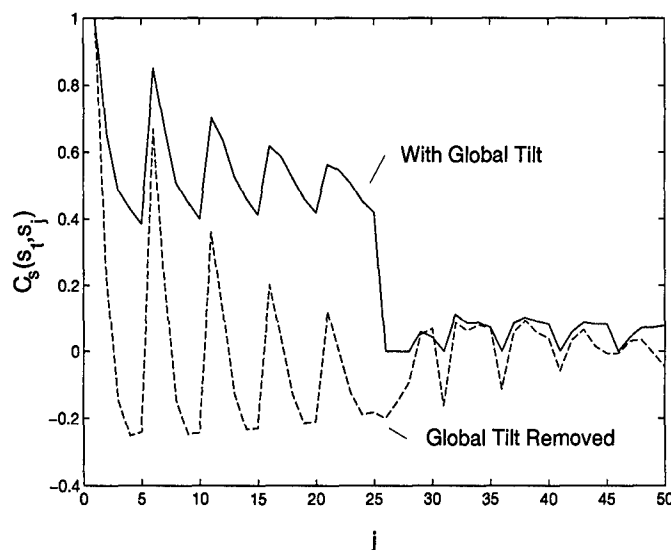


Figure 8. Comparison of slope covariance with and without global tilt. Plotted as  $C_s(s_1, s_j)$  versus  $j$  (see Fig. 2 and Eqn. (6)) where  $j$  indexes all 50 elements of the slope vector. Slope covariance shown for  $D/r_0 = 1.0$ .

is compared to the suboptimized Bayes solution. As before, the neural network performs well and approaches the suboptimized Bayes solution.

Overall, we find that both the neural network and the statistical solution for reducing the WFS mean square slope measurement error perform well in both fixed seeing conditions, and when seeing conditions are allowed to vary. However, as long as a reasonable estimate of the system mean square slope measurement error exists, the statistical solution is the better choice. Also, the removal of global tilt does reduce the amount of error reduction by both the neural network and the statistical solution due to the data being more independent. Finally, the fixed conditions tests show that a neural network can approximate the optimized Bayes solution.

*3.1.2 Reduction of WFS Slope Measurement Error Within a Single WFS Subaperture.* Another method for reducing WFS slope measurement error is to reduce the error within a single WFS subaperture. As stated in Chapter I, two effects can reduce the accuracy of slope measurements within a WFS subaperture. These effects are noise, both read

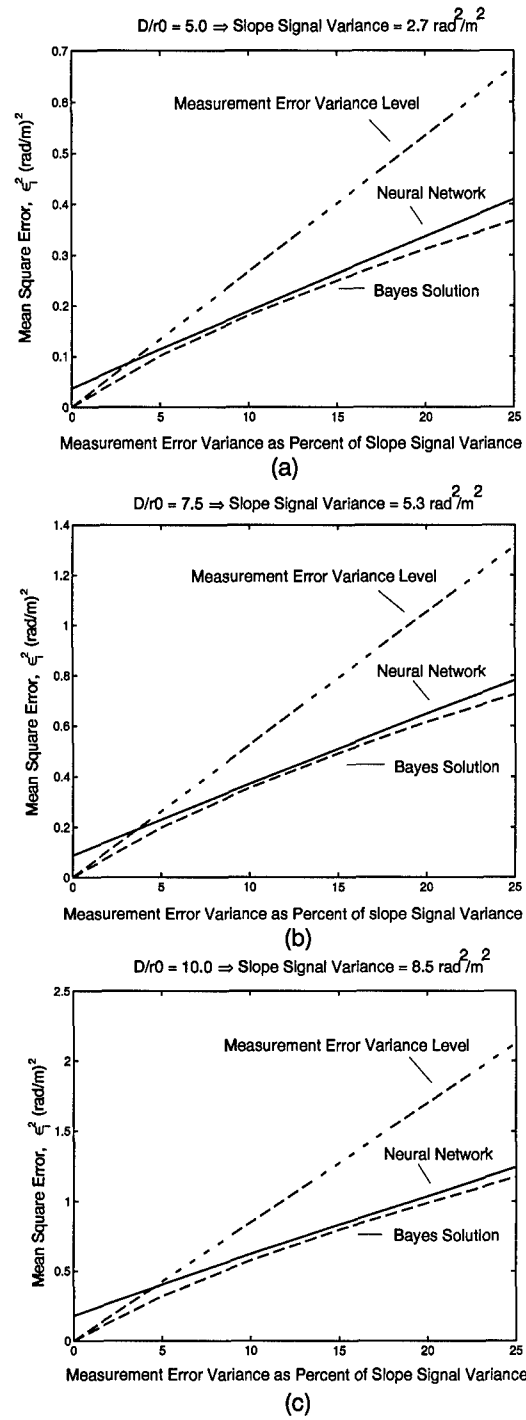


Figure 9. Comparison of neural network to Bayes optimal solution for WFS slope measurement error reduction on global tilt removed data. Average WFS slope MSE plotted versus measurement error variance for a)  $D/r_0 = 5.0$ , b)  $D/r_0 = 7.5$ , and c)  $D/r_0 = 10.0$ .

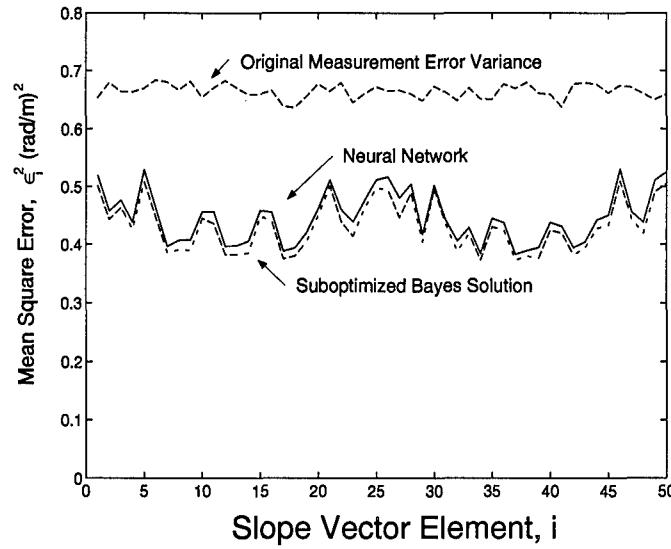


Figure 10. Average WFS slope mean square error plotted as a function of the slope measurement index (see Fig. 2) on global tilt removed data for  $D/r_0$  ranging between 5 and 10, and the WFS slope measurement error levels ranging between 0 and 25%. The three curves represent the original WFS slope measurement error level, the slope measurement error level after neural network processing, and the slope measurement error level after processing with a suboptimized Bayes solution (optimized for  $D/r_0 = 7.5$  and WFS slope measurement error level 12.5%).

and shot noise, and the problem with having spot sizes smaller than the physical dimension of an element in the detector array. Therefore, realistic WFS data are generated, and tests are conducted to compare the performance of neural networks with the standard centroid estimation technique to see if the slope measurement error can be reduced. Sets of training images are generated for a  $4 \times 4$  array of detectors with diffraction limited spot sizes of one half and one full pixel width, and for which the SNR is low, high, and infinite. Tests are conducted on the six cases shown in Table 1. In all cases phase screens of  $41 \times 41$  points are used to simulate the wavefront phase perturbations in the WFS subaperture. The true  $x$  and  $y$  centroid locations are randomly chosen from a range of  $\pm 0.5$  within a normalized aperture. For this research, the detector array is assumed to be of unit dimension and centered about the origin. Values for  $L/r_0$  are randomly chosen between 0.5 and 3.0, representing 0.5 to 3.0  $r_0$ 's per subaperture. This makes any network solution capa-

Table 1. Hartmann sensor subaperture centroid estimation test parameters: spot size and subaperture SNR.

Case	1	2	3	4	5	6
Spot Width SNR	Full Pixel $\infty$	Full Pixel High, 7.5-11.0	Full Pixel Low, 4.0-7.5	Half Pixel $\infty$	Half Pixel High, 7.5-11.0	Half Pixel Low, 4.0-7.5

ble of operating over a realistic range of atmospheric conditions. For each case, a neural network consisting of 20 hidden layer nodes and 2 linear output nodes is trained to take as input the 16 normalized detector counts, and output an estimate of both the  $x$  and  $y$  centroid locations within a normalized aperture. Once the networks are trained, new sets of data are generated for each case to compare the performance of the neural network with the conventional centroid estimator. The standard centroid estimation technique uses the following expressions to estimate the  $x$  and  $y$  centroid locations within a subaperture [29]:

$$x_c = \frac{\sum_{i=1}^N \sum_{j=1}^M x_{ij} p_{ij}}{\sum_{i=1}^N \sum_{j=1}^M p_{ij}}, \quad (19)$$

$$y_c = \frac{\sum_{i=1}^N \sum_{j=1}^M y_{ij} p_{ij}}{\sum_{i=1}^N \sum_{j=1}^M p_{ij}}, \quad (20)$$

where  $x_c$  and  $y_c$  are the  $x$  and  $y$  centroid estimates,  $N$  is the number of detectors in the  $x$  direction,  $M$  is the number of detectors in the  $y$  direction,  $x_{ij}$  is the  $x$ -direction center location of the  $ij$ th detector,  $y_{ij}$  is the  $y$ -direction center location of the  $ij$ th detector, and  $p_{ij}$  is the signal count of the  $ij$ th detector. Figures 11-16 show the results obtained for estimating the  $x$  centroid location for the six cases. The 'x' and 'o' marks represent the mean estimate for each  $x$  centroid location averaged over all data frames with the given true  $x$  centroid location. The error bars represent one standard deviation about the mean. Results for estimating the  $y$  centroid location are similar.

While both the standard centroid estimator and the neural network provide nonlinear responses across the dynamic range of the detector array, the neural network clearly provides better results than the conventional centroid estimator. The conventional centroid estimator has a fundamental limit in that it cannot yield estimates beyond the center of

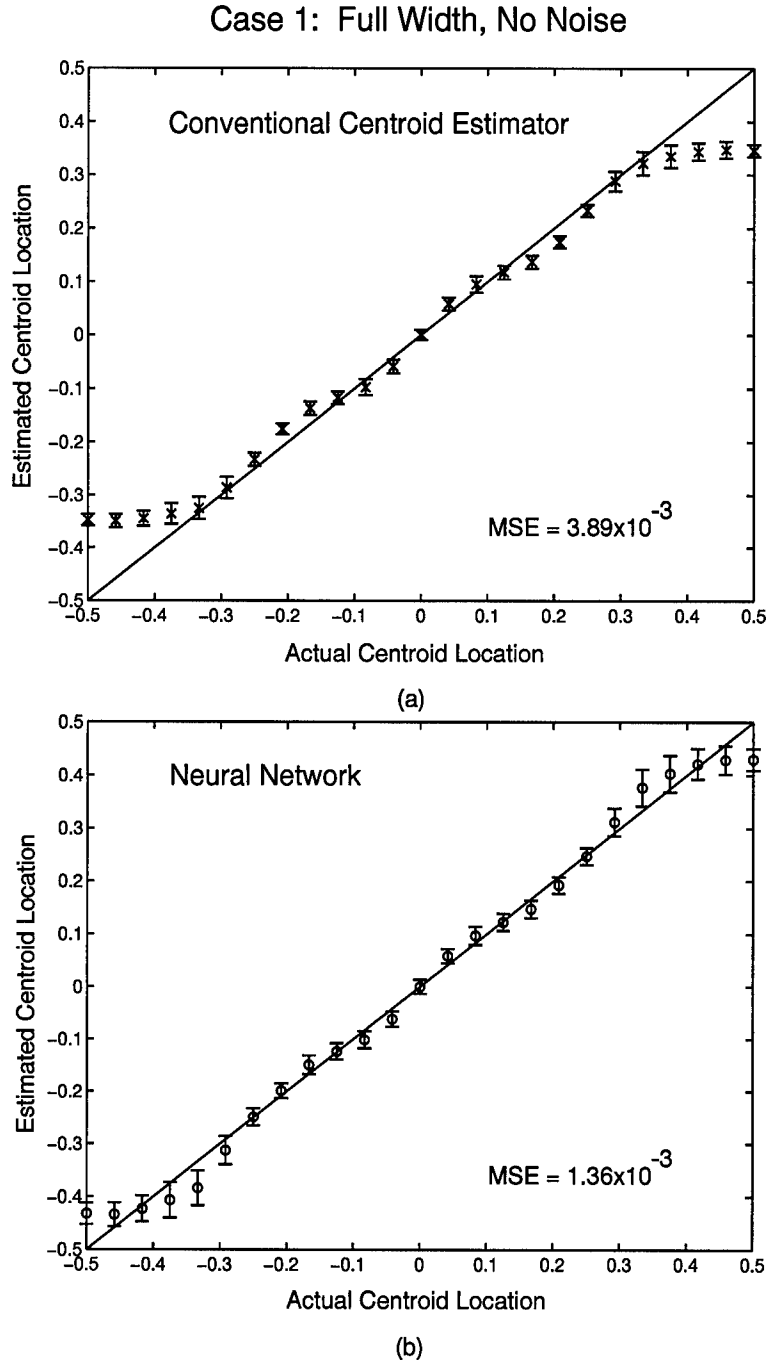


Figure 11. Comparison of WFS lenslet centroid estimation on images with main lobe the width of a single detector and no noise. Results shown for a) conventional centroid estimator, and b) neural network. Marks represent mean estimate of true centroid location, and error bars represent one standard deviation about the mean. The MSE for the conventional centroid estimator (as compared to the diagonal line in the figure) is  $3.89 \times 10^{-3}$ , while the MSE for the neural network is  $1.36 \times 10^{-3}$ .

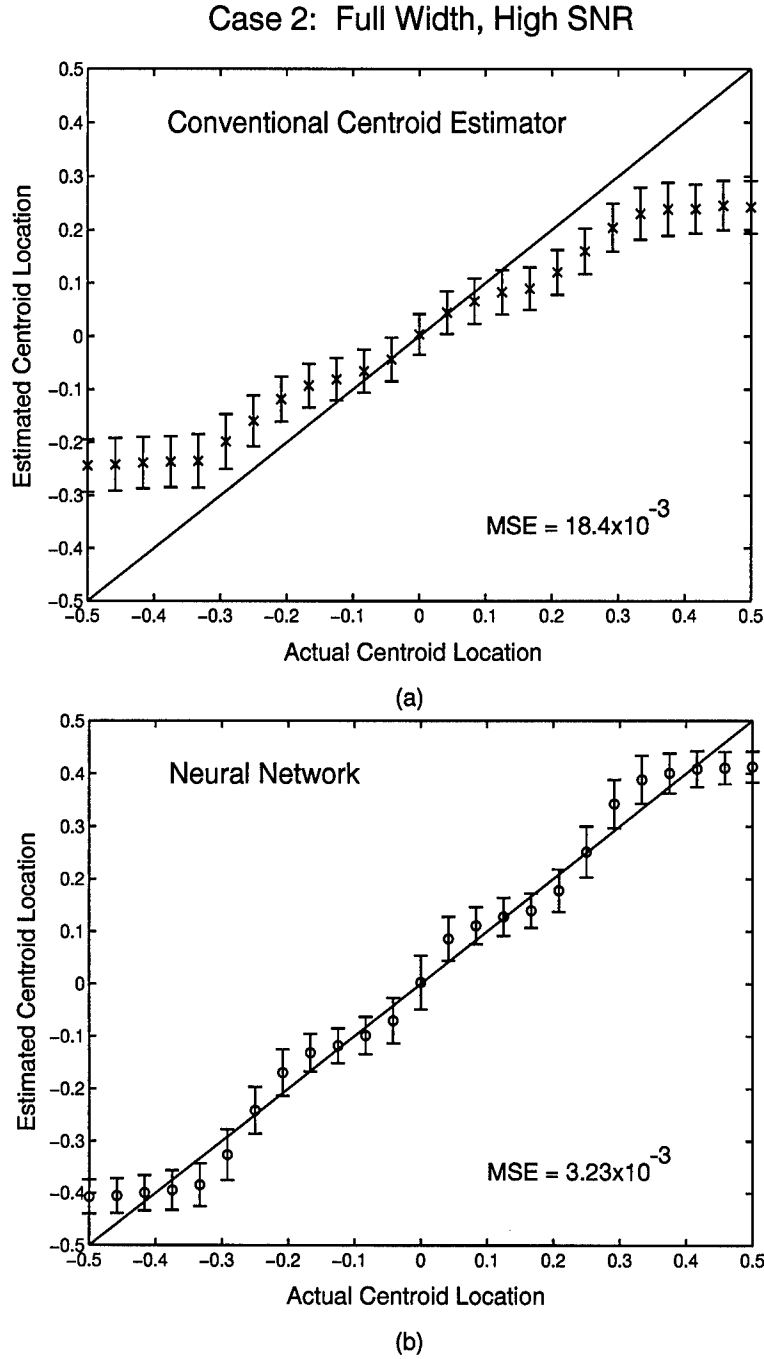
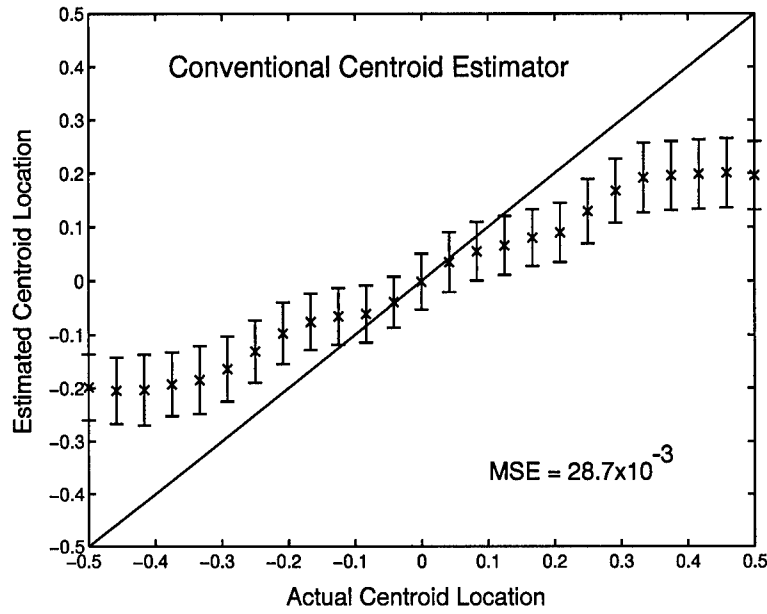
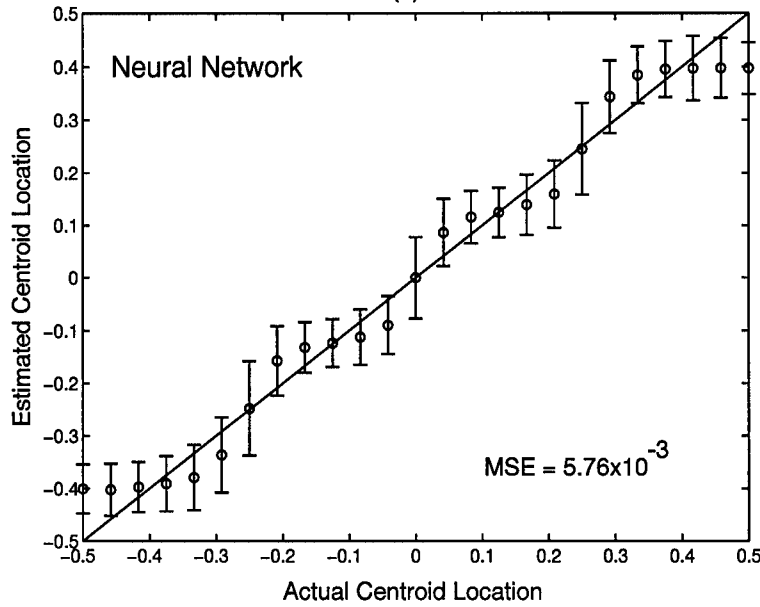


Figure 12. Comparison of WFS lenslet centroid estimation on images with main lobe the width of a single detector and SNR between 7.5 and 11.0. Results shown for a) conventional centroid estimator, and b) neural network. Marks represent mean estimate of true centroid location, and error bars represent one standard deviation about the mean. The MSE for the conventional centroid estimator (as compared to the diagonal line in the figure) is  $18.4 \times 10^{-3}$ , while the MSE for the neural network is  $3.23 \times 10^{-3}$ .

### Case 3: Full Width, Low SNR



(a)



(b)

Figure 13. Comparison of WFS lenslet centroid estimation on images with main lobe the width of a single detector and SNR between 4.0 and 7.5. Results shown for a) conventional centroid estimator, and b) neural network. Marks represent mean estimate of true centroid location, and error bars represent one standard deviation about the mean. The MSE for the conventional centroid estimator (as compared to the diagonal line in the figure) is  $28.7 \times 10^{-3}$ , while the MSE for the neural network is  $5.76 \times 10^{-3}$ .

#### Case 4: Half Width, No Noise

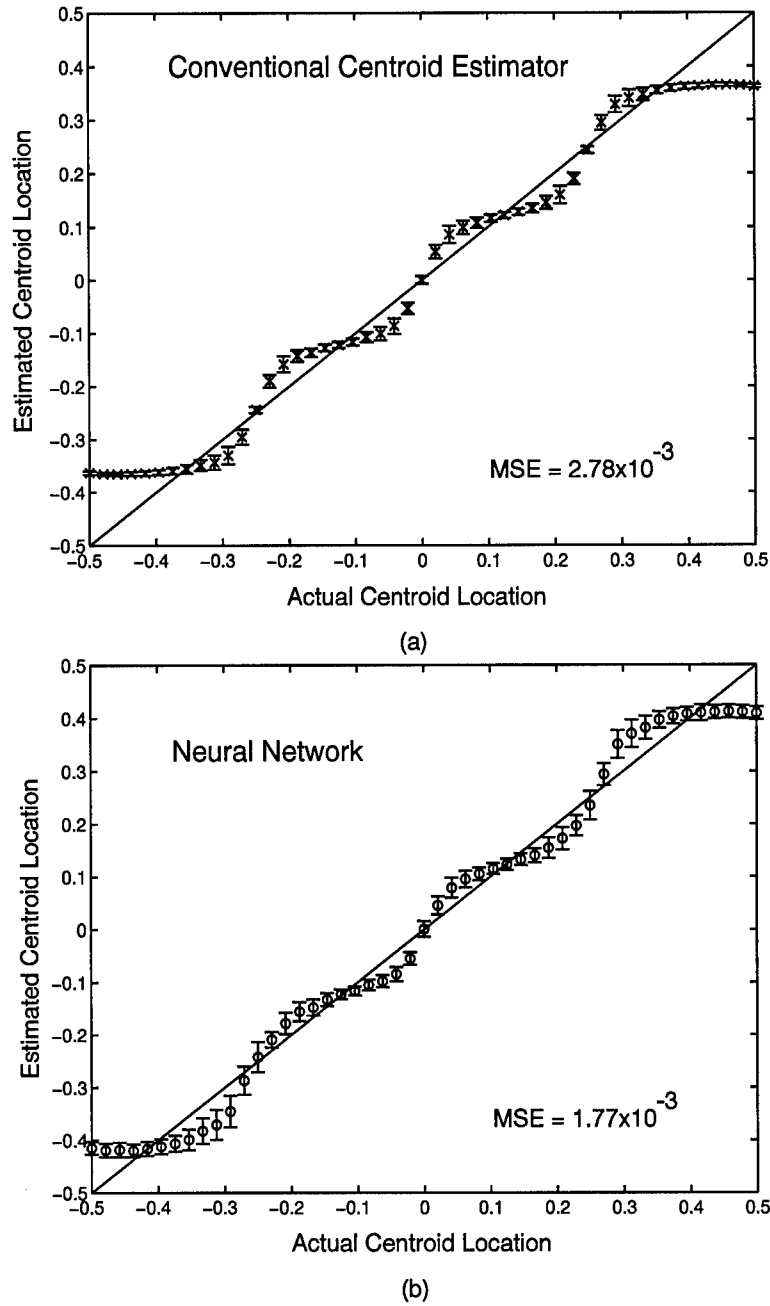
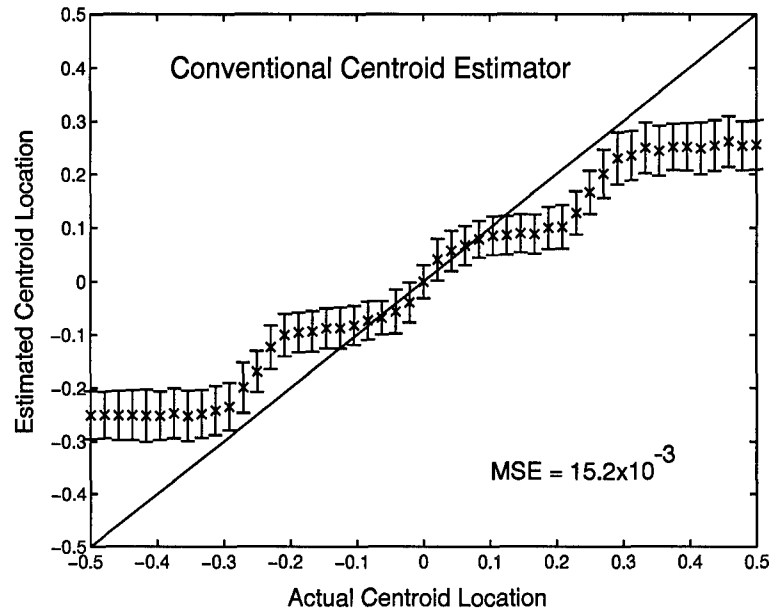
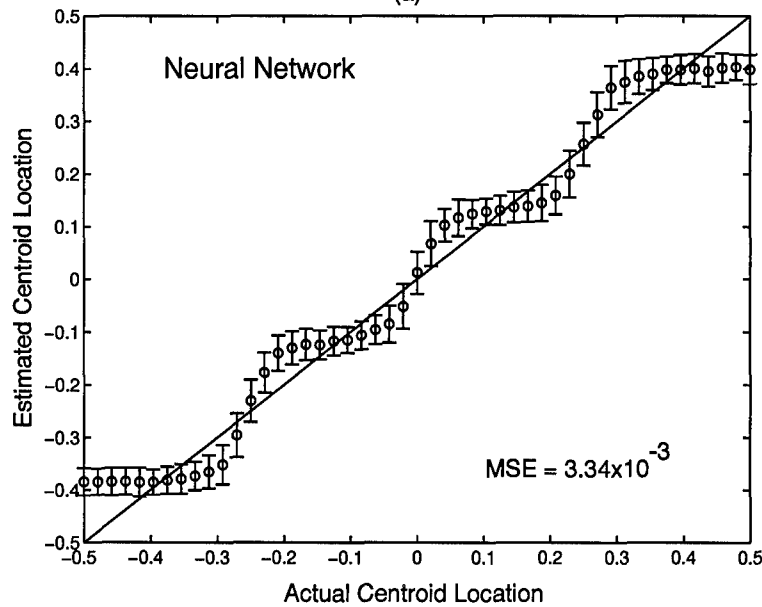


Figure 14. Comparison of WFS lenslet centroid estimation on images with main lobe half the width of a single detector and no noise. Results shown for a) conventional centroid estimator, and b) neural network. Marks represent mean estimate of true centroid location, and error bars represent one standard deviation about the mean. The MSE for the conventional centroid estimator (as compared to the diagonal line in the figure) is  $2.78 \times 10^{-3}$ , while the MSE for the neural network is  $1.77 \times 10^{-3}$ .

### Case 5: Half Width, High SNR



(a)



(b)

Figure 15. Comparison of WFS lenslet centroid estimation on images with main lobe half the width of a single detector and SNR between 7.5 and 11.0. Results shown for a) conventional centroid estimator, and b) neural network. Marks represent mean estimate of true centroid location, and error bars represent one standard deviation about the mean. The MSE for the conventional centroid estimator (as compared to the diagonal line in the figure) is  $15.2 \times 10^{-3}$ , while the MSE for the neural network is  $3.34 \times 10^{-3}$ .

### Case 6: Half Width, Low SNR

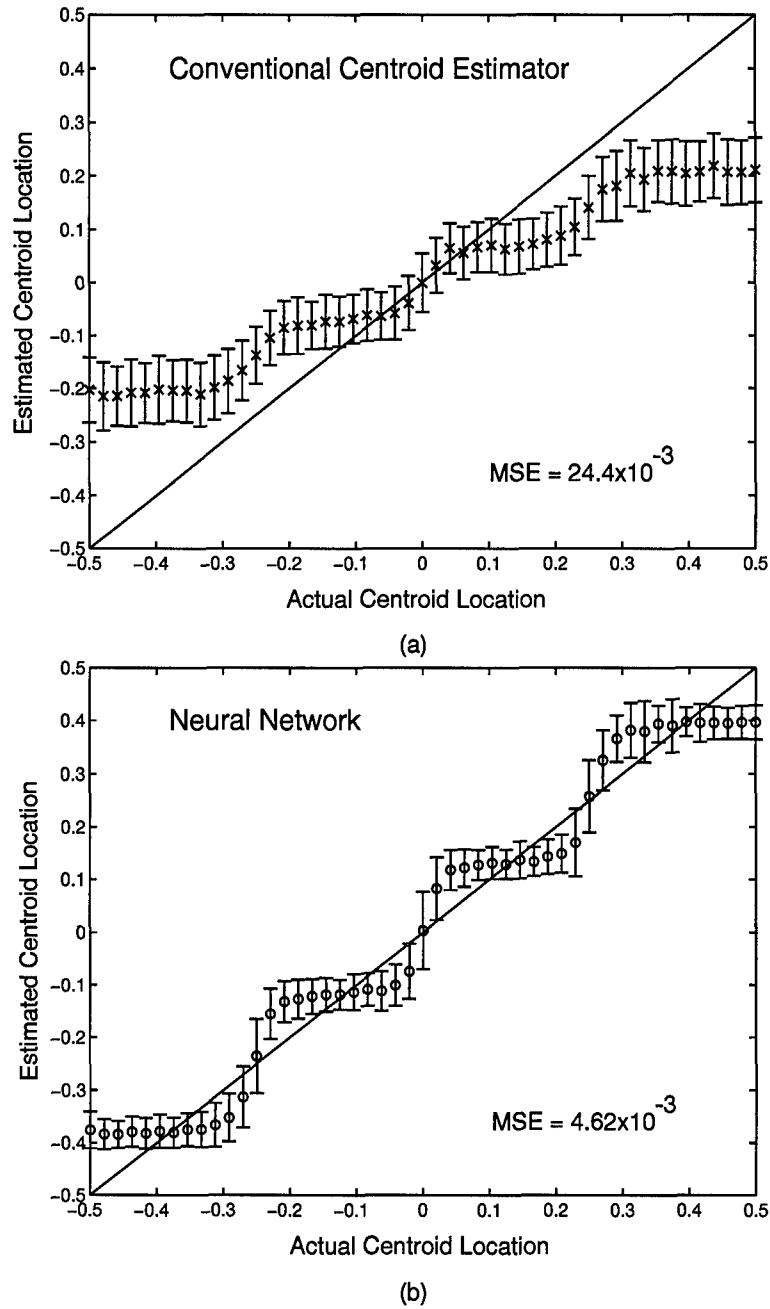


Figure 16. Comparison of WFS lenslet centroid estimation on images with main lobe half the width of a single detector and SNR between 4.0 and 7.5. Results shown for a) conventional centroid estimator, and b) neural network. Marks represent mean estimate of true centroid location, and error bars represent one standard deviation about the mean. The MSE for the conventional centroid estimator (as compared to the diagonal line in the figure) is  $24.4 \times 10^{-3}$ , while the MSE for the neural network is  $4.62 \times 10^{-3}$ .

an edge pixel. This can be seen in the noise free cases (Fig. 11 and Fig. 14). However, the neural network is able to give estimates outside the center of the edge pixels. This increase in dynamic range is also apparent in the cases with noise. The neural network also dramatically reduces the estimation error in all cases. The mean square error in centroid estimation for the neural network is between 36% and 82% less than the mean square error for the conventional centroid estimator. Finally, the neural network has a smaller deviation about the mean for each centroid location when noise is present. Figure 17 plots the standard deviation of the centroid estimator as a function of centroid location for the neural network and the conventional approach (for case 2; image main lobe = width of a detector, high SNR). In this case, the mean standard deviation for the conventional centroid estimator is  $44.9 \times 10^{-3}$  while the mean standard deviation for the neural network is  $38.9 \times 10^{-3}$ . This plot is representative of all four cases which include noise in the detectors. Figure 17 shows that the standard deviation of the neural network is smaller than that of the conventional centroid estimator over most centroid locations. The points for which the spot crosses between pixels are the only locations where the conventional centroid estimator has less standard deviation in the estimates. Overall, the neural networks provide more accurate estimates, over a larger dynamic range, and with less estimate variance.

### 3.2 WFS Slope Measurement Prediction

Even if one could eliminate WFS slope measurement error from the WFS slope measurements on which adaptive optics correction is based, the measured slopes will not perfectly match the true slopes at the time of correction due to system time delay. While correction based on these measured slopes does yield improved image quality over no correction at all, the ability to predict the true measurements at the time of correction will yield even better image quality. Therefore, tests are conducted in WFS slope measurement prediction.

To test the concept of slope prediction, two tests are conducted. The first tests data both with and without global tilt, and in fixed conditions. This test is conducted to deter-

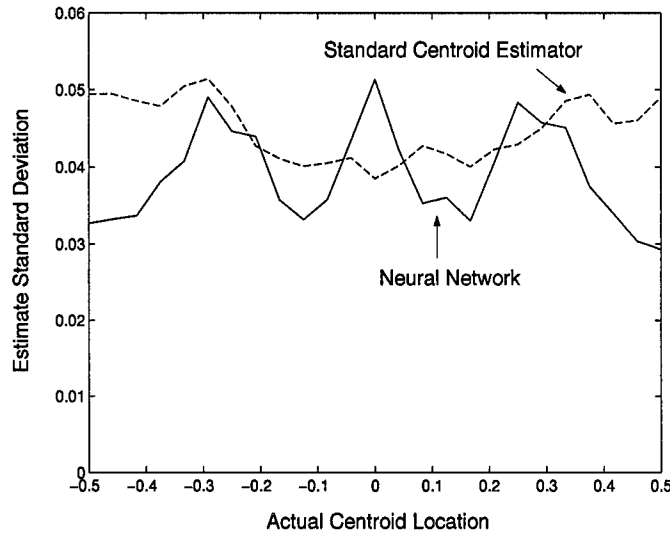


Figure 17. Comparison of standard deviation about the mean in WFS lenslet centroid estimation on images with main lobe the width of a single detector and SNR between 7.5 and 11.0.

mine if neural networks can perform prediction at all. If neural networks cannot perform prediction under fixed seeing conditions, then they will not be able to perform prediction when seeing conditions are varying. This test also shows how well a neural network can approximate the optimized Bayes solution (see Eqn. (4)). The second test is conducted under varying conditions, again on data with and without global tilt. This test represents how well neural networks will perform prediction under real world conditions. Because seeing conditions are continually changing, any viable prediction scheme must be able to operate over a useful range of conditions. For this test,  $D/r_0$  is allowed to vary between 5-20, WFS slope measurement error is allowed to vary between 0-25% of the wavefront slope variance, and the  $x$  and  $y$  wind speeds of each layer are allowed to range from  $\pm 0.1D$  per frame. This test shows the ability of neural networks to function in more realistic conditions and still provide benefit. Because a single frame of slope measurements contains no information about the atmospheric wind speeds, and thus the temporal evolution of the atmosphere, prediction based on a single frame of slope measurements is not possible unless the wind speeds are fixed and known. Since a key issue of this research is to find

robust solutions which operate over broad ranges of conditions, including wind speeds, a set of slope measurements is predicted based on the previous two frames of measured slope data in this research.

For the “fixed conditions” test, neural networks are trained to take as input the 100 slope measurements from the previous two frames, and output the 50 slope measurements of the current frame. The value of  $D/r_0$  is set at 1.0, and the four layer wind speed profile found in Table 2 is used. The signal is set to be noise free to determine if neural network prediction is even possible without the complications of noise. Sets of slope measurements representing three consecutive frames of data with the proper spatial and temporal statistics are generated to train the neural networks. Independent sets of similar data are generated to test the neural networks and the statistical predictors. In both cases, a neural network with 80 hidden nodes and 50 linear output nodes is trained to perform prediction. Figures 18 and 19 show the results obtained from both the neural networks and the Bayes predictors. Results show the MSE between the true current slope measurements and the predicted slope measurements as given by Eqn. (17). Also shown in the figures are the variances of the current true slopes (representing no correction), and the MSE between the current true slopes and the previous frame of measured data (representing correction based solely on the previously measured slopes). Correction based solely on the previously measured slopes represents the residual slope MSE if correction of the current true slopes is based on deformable mirror settings which would perfectly correct the previously measured slopes. The MSE is plotted as a function of the index of the 50 WFS slopes (see Fig. 2). Figures 18 and 19 clearly show that predictive techniques do reduce the MSE between the true slope measurements and those that would be used for correction if prediction is not used, and that the neural networks do approximate the optimized Bayes solution when conditions are fixed. In the case with global tilt, correction based on the previous frame reduces the slope MSE by 82%, correction based on neural network prediction reduces the slope MSE by 94%, and correction based on the optimized Bayes predictor reduces the slope MSE by 94%. Therefore, prediction reduces the MSE of correction based on the previous

Table 2. Four layer wind speed profile for fixed conditions prediction tests. Wind speeds are given per frame time.

Layer	$x$ Wind Speed	$y$ Wind Speed
1	$0.1D$	$0.0D$
2	$0.0D$	$0.1D$
3	$-0.1D$	$0.0D$
4	$0.0D$	$-0.1D$

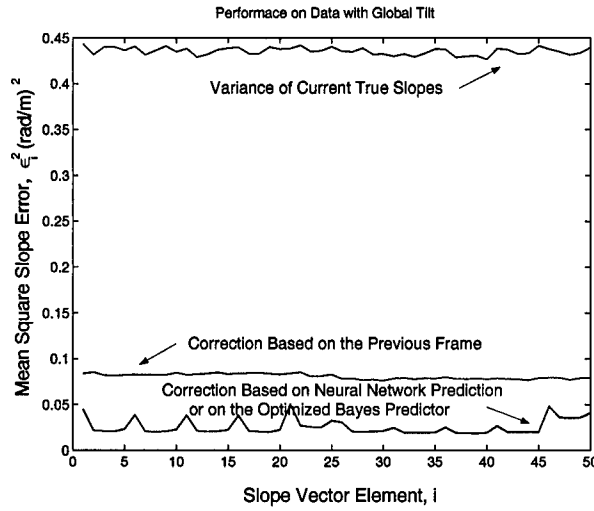


Figure 18. Mean square slope error,  $\epsilon_i^2$ , plotted as a function of WFS slope index  $i$  (see Fig. 2) on data with global tilt. Also shown are the variances of the current true slopes. Parameters fixed at  $D/r_0 = 1.0$ , no noise, and wind speed profile fixed (see Table 2).

frame by 67%. When global tilt is removed, correction based on the previous frame reduces the slope MSE by 53%, correction based on neural network prediction reduces the slope MSE by 85%, and correction based on the optimized Bayes predictor reduces the slope MSE by 86%. Therefore, prediction on data with global tilt removed reduces the MSE of correction based on the previous frame by 68%. The structure on the results in Figs. 18 and 19 from either the neural network predictor or the optimized statistical predictor are as expected. The best prediction is accomplished on slope elements representing center pixels (see Fig. 2), while edge and corner pixels have larger residual errors.

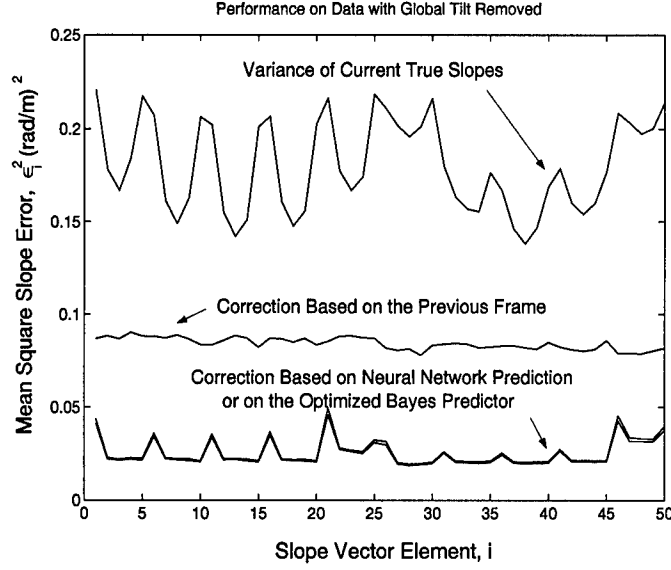


Figure 19. Mean square slope error,  $\epsilon_i^2$ , plotted as a function of WFS slope index  $i$  (see Fig. 2) on data with global tilt removed. Also shown are the variances of the current true slopes. Parameters fixed at  $D/r_0 = 1.0$ , no noise, and wind speed profile fixed (see Table 2).

For the “varying conditions” test, neural networks are again trained to take as input the 100 slope measurements from the previous two frames, and output the 50 slope measurements of the current frame. For each sequence of three frames (2 for inputs and 1 as output) random values for  $D/r_0$ , slope measurement error, and the wind speed profile are chosen. The value of  $D/r_0$  is chosen between 5-20 representing from 1 to 4  $r_0$ ’s per subaperture. Slope measurement error is randomly chosen in the range of 0-25% of the wavefront slope variance. The  $x$  and  $y$  wind speeds of each of the four layers are randomly chosen between  $\pm 0.1D$  per frame. Sets of slope measurements representing three consecutive frames of data with the proper spatial and temporal statistics are generated to train the neural networks. Error is only added to the first two frames (inputs to the neural network) while the third frame is Error free. Independent sets of data are generated to test the neural networks and the statistical predictors. In the case of slopes with global tilt, a neural network with 200 hidden nodes and linear output nodes is trained to perform prediction. Figure 20 shows the MSE results. In the case of slopes where global tilt is removed, a neural network

with 160 hidden nodes is used. Figure 21 shows the result obtained on global tilt removed data. In both graphs, the MSE between the true current slopes and the predicted slopes is shown. Also shown in the figures are the variances of the current true slopes (representing no correction), and the MSE between the current true slopes and the previous frame of measured data (representing correction based solely on the previously measured slopes). The MSE,  $\epsilon_i^2$ , is plotted as a function of the index,  $i$ , of the 50 WFS slopes (see Fig. 2). Figures 20 and 21 clearly show that using a single neural network for prediction reduces the MSE between the true slopes and those that would be used for correction, even if the seeing conditions are allowed to vary over a broad range. In the case with global tilt, correction based on the previous frame reduces the slope MSE by 75%, and correction based on neural network prediction reduces the slope MSE by 79%. The results based on neural network prediction represent a 16% decrease in MSE from correction based solely on the previous frame. When global tilt is removed, correction based on the previous frame reduces the slope MSE by 56%, and correction based on neural network prediction reduces the slope MSE by 68%. For global tilt removed data, the results based on neural network prediction represent a 27% decrease in MSE from correction based solely on the previous frame.

To understand the impact of varying seeing conditions on Bayes prediction, a test is conducted on the global tilt removed data. The statistical predictor is set for the mean seeing conditions ( $D/r_0 = 12.5$  and noise variance set at 12.5% of signal variance), and three tests are conducted each with set wind speeds. The wind speeds within the fixed Bayes predictor are all set at  $0.0D$  per frame in the first case,  $0.05D$  in the second case, and  $0.1D$  in the third case, while the wind speeds of the test data are allowed to vary between  $\pm 0.1D$  per frame. For each case the Bayes solution is generated, and then the entire set of test data, covering the full range of parameters, is used to test the fixed Bayes predictor. Again,  $D/r_0$  is between 5-20, noise is from 0-25% of signal variance, and the  $x$  and  $y$  wind speeds are chosen between  $\pm 0.1D$  per layer. The results of these three cases are shown in Figs. 22-24. These graphs show that correction based on a fixed Bayes solution while seeing conditions are allowed to vary yields significantly degraded MSE than just correcting based on the

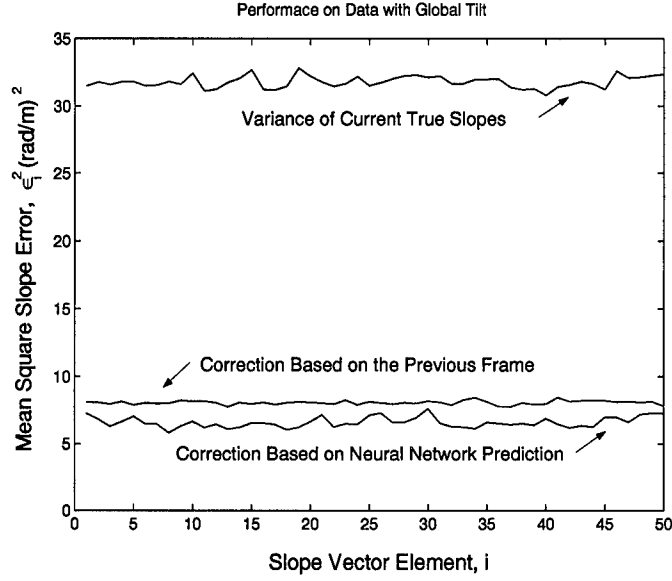


Figure 20. Mean square slope error,  $\epsilon_i^2$ , plotted as a function of WFS slope index  $i$  (see Fig. 2) on data with global tilt. Also shown are the variances of the current true slopes. Parameters varying with  $D/r_0$  between 5-20, noise variance between 0-25% of slope signal variance, and  $x$  and  $y$  wind speeds between  $\pm 0.1D$  per layer.

previous frame. For the case of wind speeds set at  $0.05D$ , correction based on the previous frame reduces the slope MSE by 56%, and correction based on neural network prediction reduces the slope MSE by 68%. However, correction based on the fixed statistical predictor only reduces the slope MSE by 48%. Therefore, while prediction with the neural network reduces the MSE versus correction based on the previous frame by 27%, prediction with the fixed Bayes predictor increases the MSE versus correction based on the previous frame by 18%. Because the statistical predictor relies on the structure of the slope covariance function, and because the structure of the slope covariance function is dependent on the wind speed chosen, we find that prediction with the Bayes predictor when the wind speeds are not known results in a decrease in performance when compared to correction based on the previous frame of slope measurements. Since knowing the current seeing conditions is not always possible, this indicates that neural networks are clearly the better way to perform prediction.

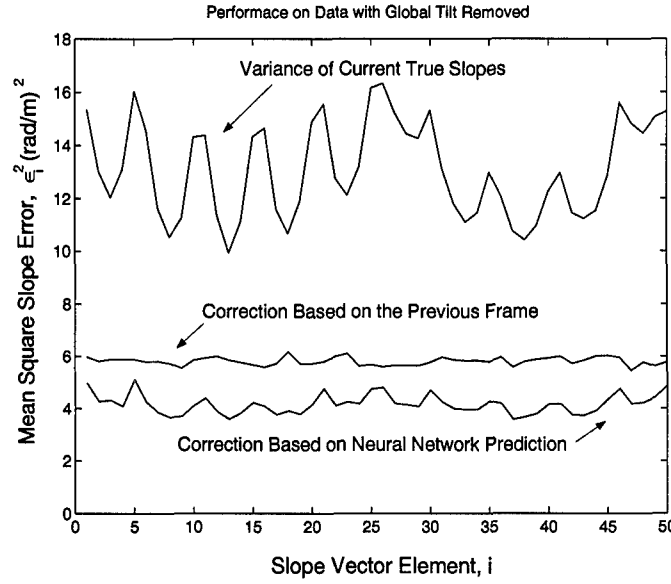


Figure 21. Mean square slope error,  $\epsilon_i^2$ , plotted as a function of WFS slope index  $i$  (see Fig. 2) on data with global tilt removed. Also shown are the variances of the current true slopes. Parameters varying with  $D/r_0$  between 5-20, noise variance between 0-25% of slope signal variance, and  $x$  and  $y$  wind speeds between  $\pm 0.1D$  per layer.

Another test is conducted to see if neural networks can increase the maximum wind speed under which adaptive optics provide benefit. As was stated in Chapter II, for the lenslet array configuration used in this research, the maximum wind speed under which correction based solely on previous measured data improves image quality is  $0.1D$  per frame when global tilt is removed from the data. Therefore, a test is conducted under varying conditions to see if prediction with a neural network can provide benefit on data with wind speeds up to  $0.2D$  per frame. For this test,  $D/r_0$  is between 5-20, noise is from 0-25% of signal variance, and the  $x$  and  $y$  wind speeds are chosen between  $\pm 0.2D$  per layer. Figure 25 shows the results obtained. Overall, correction based on the previous frame reduces the slope MSE by 5%, while correction based on neural network prediction reduces the slope MSE by 43%. This plot shows that on the average, correction based on the previous frame is no better than no correction at all when wind speeds are allowed

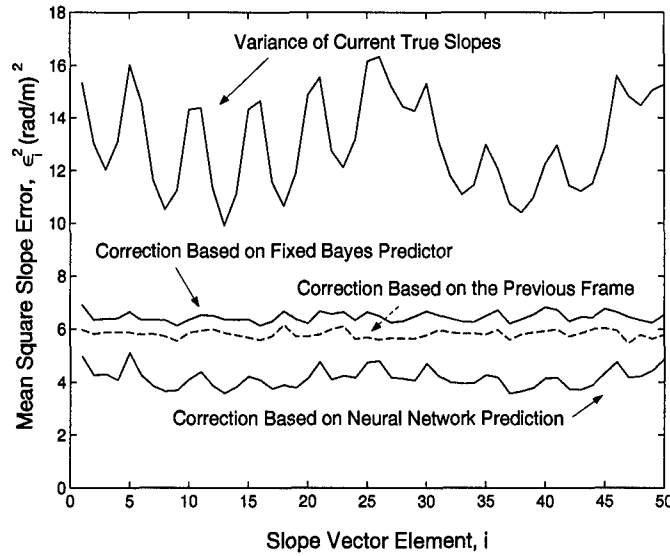


Figure 22. Mean square slope error,  $\epsilon_i^2$ , plotted as a function of WFS slope index  $i$  (see Fig. 2) on data with global tilt removed. Also shown are the variances of the current true slopes. Signal parameters varying with  $D/r_0$  between 5-20, noise variance between 0-25% of slope signal variance, and  $x$  and  $y$  wind speeds between  $\pm 0.1D$  per layer. Statistics based predictor fixed for  $D/r_0 = 12.5$ , noise variance 12.5% of slope signal variance, and all wind speeds set at  $0.0D$  per frame.

to vary between  $\pm 0.2D$  per frame, while prediction with a neural network still improves system performance.

A final test is conducted to understand the added benefit of using the previous three frames as inputs to neural networks as compared to just the previous two. Training data with global tilt is generated for  $D/r_0 = 1.0$ , no noise, and wind speeds limited to  $\pm 0.1D$  per frame. A neural network with 80 hidden layer nodes is trained to take the previous two frames of slope measurements as input, and to predict the current frame as output. Another network with 80 hidden layer nodes is trained to take the previous three frames as input, and to predict the current frame of slope measurements as output. The results of both networks are shown in Fig. 26. Correction based on the previous frame reduces the slope MSE by 87%, while correction based on neural network prediction with 2 frames as inputs reduces the slope MSE by 92%, and correction based on neural network prediction

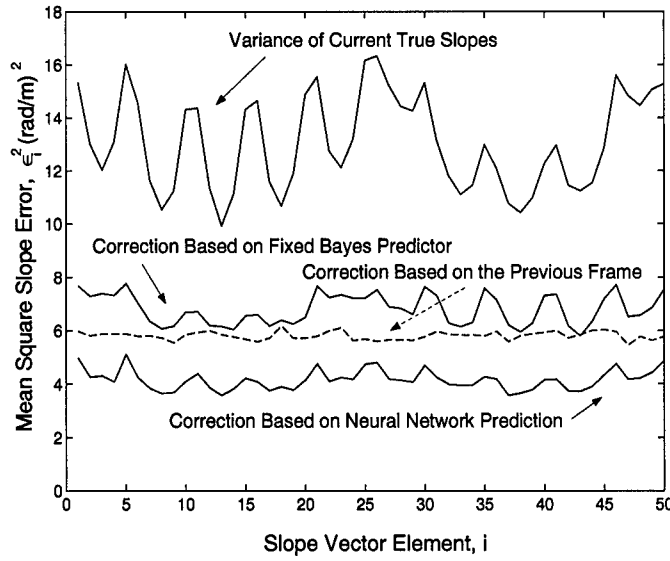


Figure 23. Mean square slope error,  $\epsilon_i^2$ , plotted as a function of WFS slope index  $i$  (see Fig. 2) on data with global tilt removed. Also shown are the variances of the current true slopes. Signal parameters varying with  $D/r_0$  between 5-20, noise variance between 0-25% of slope signal variance, and  $x$  and  $y$  wind speeds between  $\pm 0.1D$  per layer. Statistics based predictor fixed for  $D/r_0 = 12.5$ , noise variance 12.5% of slope signal variance, and all wind speeds set at  $0.05D$  per frame.

with 3 frames as inputs reduces the slope MSE by 93%. Although the additional frame of inputs to the network does improve prediction performance, the improvement is small considering the additional processing required.

Along with system time delay, anisoplanatism, or separation between the beacon and the object of interest, can be a major factor in adaptive optics system performance. Under anisoplanatic conditions, errors occur in wavefront correction based on the difference in paths. Anisoplanatism can be modeled in the slope covariance expression by substituting  $+z_k(\theta_1 - \theta_2)$  for  $-\vec{v}(z_k)(t_1 - t_2)$  into Eqn. (6), where  $\theta_1$  and  $\theta_2$  represent the angles between the normal to the telescope pupil and the beacon or object of interest [18]. This substitution yields the following expression for the covariance between any two slopes:

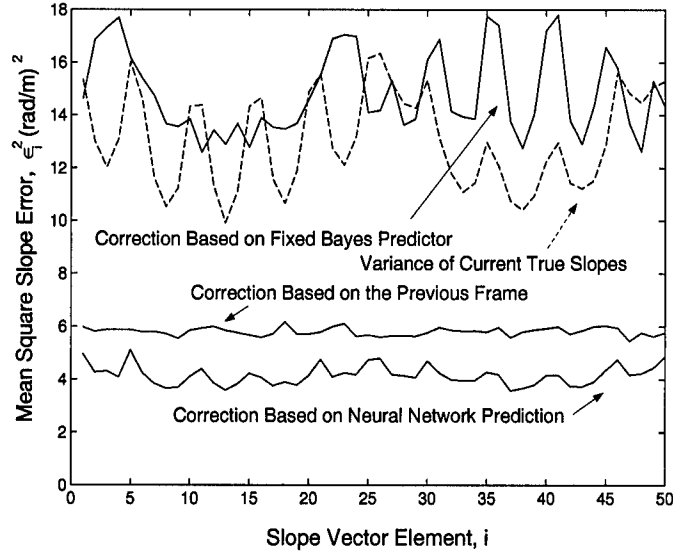


Figure 24. Mean square slope error,  $\epsilon_i^2$ , plotted as a function of WFS slope index  $i$  (see Fig. 2) on data with global tilt removed. Also shown are the variances of the current true slopes. Signal parameters varying with  $D/r_0$  between 5-20, noise variance between 0-25% of slope signal variance, and  $x$  and  $y$  wind speeds between  $\pm 0.1D$  per layer. Statistics based predictor fixed for  $D/r_0 = 12.5$ , noise variance 12.5% of slope signal variance, and all wind speeds set at  $0.1D$  per frame.

$$\begin{aligned}
 C_s(s_i(\theta_1), s_j(\theta_2)) &= E[s_i(\theta_1)s_j(\theta_2)] \\
 &= -3.44 \left(\frac{D}{r_0}\right)^{\frac{5}{3}} \sum_{k=1}^N f(z_k) \\
 &\quad \times \int \int d\vec{x}_1 d\vec{x}_2 w_i^s(\vec{x}_1) w_j^s(\vec{x}_2) |\vec{x}_1 - \vec{x}_2 + z_k(\theta_1 - \theta_2)|^{\frac{5}{3}},
 \end{aligned} \tag{21}$$

where  $s_i(\theta)$  is the slope in the  $i$ th subaperture from the object at angle  $\theta$ . In essence, this substitution has added a fixed wind speed velocity at each layer between the beacon and the object of interest. Therefore, we can draw conclusions about compensating for anisoplanatic effects from the results of the temporal prediction tests. First, neural networks should

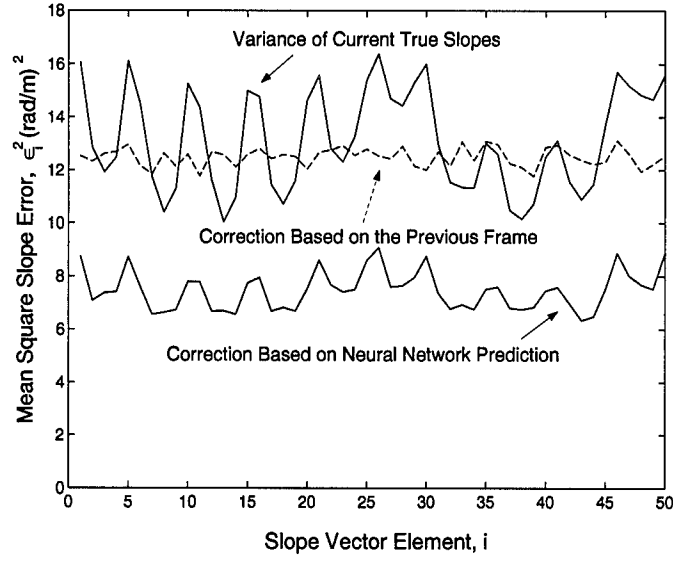


Figure 25. Mean square slope error,  $\epsilon_i^2$ , plotted as a function of WFS slope index  $i$  (see Fig. 2) on data with global tilt removed. Also shown are the variances of the current true slopes. Signal parameters varying with  $D/r_0$  between 5-20, noise variance between 0-25% of slope signal variance, and  $x$  and  $y$  wind speeds between  $\pm 0.2D$  per layer.

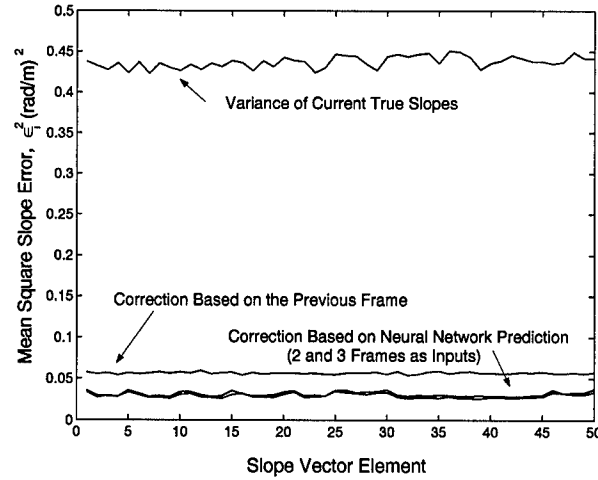


Figure 26. Mean square slope error,  $\epsilon_i^2$ , plotted as a function of WFS slope index  $i$  (see Fig. 2). Also shown are the variances of the current true slopes. Signal parameters of  $D/r_0 = 1.0$ , no noise, and  $x$  and  $y$  wind speeds between  $\pm 0.1D$  per layer.

be able to improve performance by predicting the wavefront structure from the object of interest based on the wavefront structure from the beacon. Also, because the “wind speeds” are fixed due to a fixed anisoplanatic angle, a statistical predictor should be capable of compensating for the anisoplanatic effects. Applying the anisoplanatic case to Eqn. (4) yields

$$\hat{x}_o = Ax_b, \quad (22)$$

where  $\hat{x}_o$  is the vector of estimated slopes associated with the object wavefront, and  $x_b$  is the vector of measured slopes from the beacon. The matrix  $A$  is found by solving

$$A = R_{oo}^{-1}R_{bo}, \quad (23)$$

where  $R_{oo}$  is the covariance matrix of the object wavefront slopes, and  $R_{bo}$  is the covariance matrix for the beacon and the object wavefront slopes.

Overall, we find for temporal prediction that when seeing conditions are set, a neural network solution will approximate an optimized Bayes solution. We find that a single neural network can be trained to perform under a broad range of seeing conditions, and that a single fixed statistical solution cannot provide benefit under those same conditions. Prediction based on slope data with global tilt removed produces a larger error as a percentage of the uncorrected signal variance than prediction based on slope data with global tilt. However, the gain in correction between correction based solely on the previous frame and correction based on prediction is more significant for data with global tilt removed. Finally, we see that prediction with a neural network can allow adaptive optics to function under a larger set of wind speeds than a system without prediction. Overall, neural networks offer a viable solution for prediction of WFS slope measurements which helps compensate for system time delay.

## IV. Key Parameter Estimation

While improving the accuracy of WFS slope measurements should yield significant improvements in adaptive optics image quality, another key to improving the performance of adaptive optics systems is in estimating key atmospheric and system parameters. These parameters include the Fried coherence length,  $r_0$ , the atmospheric wind speed profile, the strength of the atmospheric turbulence layers, and the WFS mean square slope estimation error. Real time knowledge of these parameters would improve the performance of optimized wavefront reconstruction algorithms. However, the ability to maintain an accurate estimate of these parameters in real time has not been demonstrated.

### 4.1 Estimation of $r_0$

One parameter of particular interest to adaptive optics is the Fried coherence length  $r_0$ . Knowledge of this parameter is crucial to the performance of statistical based techniques for wavefront reconstruction such as the minimum variance reconstructor [24]. Knowledge of  $r_0$  also benefits conventional techniques for estimating other key parameters such as WFS mean square slope measurement error, and conventional techniques for reducing the WFS slope measurement error. Because the covariance of the WFS slope measurements is directly related to  $(D/r_0)^{\frac{5}{3}}$  as seen in Eqn. (6), Page 16, the neural networks in this research are trained to estimate the ratio  $(D/r_0)$ .

For comparison, a conventional method for estimating  $D/r_0$  is developed. In this conventional method the variance of the WFS measurements is estimated using a specified number of WFS measurement frames. If the WFS measurements are corrupted by errors due to the measurement process, the variance of the measurement error is assumed known and subtracted from the measured signal variance. Because the variance of a single slope

measurement is proportional to  $(D/r_0)^{\frac{5}{3}}$ , as seen in Eqn. (6),  $D/r_0$  is estimated using

$$\frac{\sigma_s^2 \left( \text{calculated from measured data for unknown } \frac{D}{r_0} \right)}{\sigma_s^2 \left( \text{calculated from Eqn. (6) with } \frac{D}{r_0} = 1.0 \right)} = (\hat{D}/r_0)^{\frac{5}{3}}, \quad (24)$$

where  $\sigma_s^2$  is the variance of the WFS slopes for a given  $D/r_0$ . We refer to estimating  $D/r_0$  via Eqn. (24) as the “variance based technique.”

To test the concept of  $D/r_0$  estimation from WFS measurements, two experiments are conducted. The first experiment assumes noise free conditions, while the second includes WFS error in the measurements. For both experiments, a range of  $D/r_0$  is chosen. A range of  $D/r_0 = 5$  to 20 is used since it corresponds to 1 to 4  $r_0$ ’s per subaperture in the WFS. A neural network consisting of 60 hidden layer nodes and a single, nonlinear sigmoid node, is trained to take as inputs the 50 noise free WFS measurements from each frame, and estimate  $(D/r_0)$  as its output. Independent test sets of slope screens are then generated, again using  $D/r_0$  in a range of 5 to 20, to compare the performance of the neural network to the variance based estimator. In order to test the neural network against the variance based technique, the test sets are generated in the following manner. First, 1000 values of  $D/r_0$  are randomly selected from the range of 5 to 20. Next,  $M$  realizations of the WFS measurements are generated for each selected value of  $D/r_0$ . Then, each of the  $M$  realizations for a particular  $D/r_0$  is used to estimate  $D/r_0$  via the neural network and the covariance based estimator. The estimate of  $D/r_0$  is averaged over the  $M$  values. Finally, the mean square error (MSE) of the 1000  $D/r_0$  estimates is plotted versus  $M$ . The MSE is calculated using

$$\epsilon^2 = \frac{1}{1000} \sum_{j=1}^{1000} \left( \left( \frac{\hat{D}}{r_0} \right)_j - \left( \frac{D}{r_0} \right)_j \right)^2, \quad (25)$$

where  $(D/r_0)_j$  is the known true value,  $(\hat{D}/r_0)_j$  is the estimate,

$$\left( \frac{\hat{D}}{r_0} \right) = \frac{1}{M} \sum_{k=1}^M \left( \frac{\tilde{D}}{r_0} \right)_k, \quad (26)$$

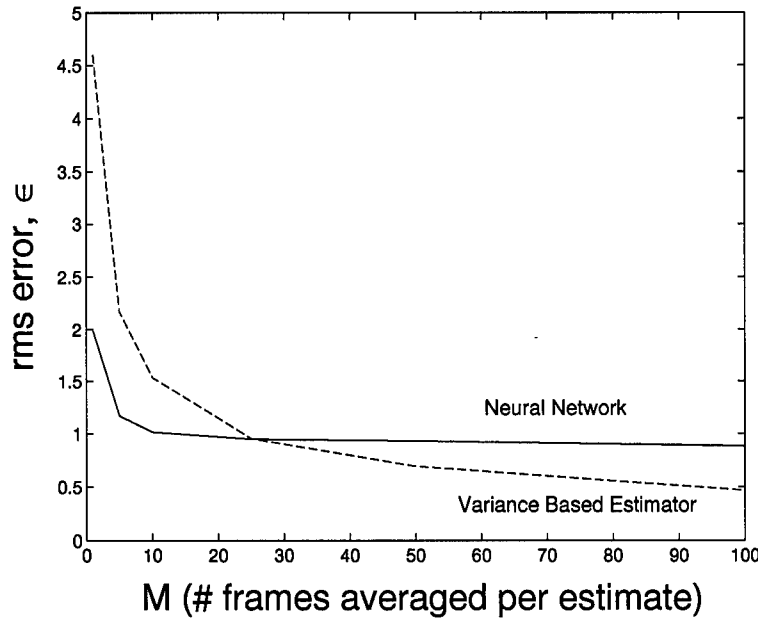


Figure 27. Comparison of the neural network and variance based technique for noise free  $D/r_0$  estimation. RMS error plotted versus  $M$ , the number of frames averaged per  $D/r_0$  value. The RMS error is averaged over 1000 randomly selected values of  $D/r_0$  ranging from 5-20.

and  $(\tilde{D}/r_0)_k$  is a single estimate from a single frame of WFS data. The performance results for each method, plotted as rms error versus  $M$ , are shown in Fig. 27 for the case of zero noise. The break even point in performance between the neural network and the variance based estimator is around 25 frames. When estimates are based on the average of more than 25 frames of WFS measurements, sufficient data are available for the variance based estimator to achieve a better estimate of  $D/r_0$ .

The noise free experiment shows that the neural network can provide performance similar to that obtained using the variance based technique. However, a more realistic test is in how each method performs in the presence of noise. A new set of training data is generated with all the same parameters as the noise free test. However, to determine if neural networks are flexible in the presence of noise, independent Gaussian noise, used to model WFS slope measurement error, is added to the slopes. Because the actual WFS mean square slope measurement error is not normally known for any frame of data, the

neural network must be flexible enough to operate over a range of error levels. For this experiment, a random measurement error is added to the slopes. The variance of the error ranges from 0-25% of the slope variance (error level 0-25%). This range corresponds to a signal to noise ratio (SNR) of 4 and greater. Since the signal variance is dependent on the value of  $D/r_0$  (see Eqn. (6)), the actual variance of the slope measurement error is also dependent on the  $D/r_0$  selected. The actual percent error added is randomly selected for each generated slope screen from a uniform distribution across the 0-25% range. A neural network consisting of 140 hidden layer nodes and a single, nonlinear sigmoid node, is again trained to estimate  $(D/r_0)$ . Like the noise free experiment, the net is trained to take as input a single 50 element set of WFS data, and output an estimate of  $D/r_0$ . Independent sets of slope screens are then generated, again using  $D/r_0$  in a range of 5 to 20, and WFS slope measurement error level in the range of 0-25%. Separate test sets are generated to compare the performance of the neural network with the variance based estimator. Like the noise free experiment, results are averaged over  $M$  frames to determine where the performance curves of each method cross. For comparison, the performance of the neural network is compared to three forms of the variance based method. In the first variance based method, perfect knowledge of the variance of the slope measurement error for each frame of test data is assumed. Therefore, the results of this method represent the best variance based  $D/r_0$  estimator. The second variance based method represents a "level playing field" with the neural network. Since the neural network is provided no information about the measurement error level of each frame, it is logical to test a variance based method based on the same lack of information. Therefore, the mean square slope measurement error used in the variance based calculation is assumed to be a single value regardless of the true error variance. The error level is assumed to be 12.5% of the signal variance (mean error level) for  $D/r_0 = 12.5$  (mean signal level). The third variance based method is based on using the "best guess" of the mean square slope measurement error as determined by a neural network. In Section 4.4, we show that a neural network is able to estimate the slope measurement error level within a MSE of  $0.035\text{rad}^2/\text{m}^2$ . Therefore, for

each frame of data, the actual measurement error level is assumed known to within a MSE of  $0.035\text{rad}^2/\text{m}^2$ . The variance of the signal is then estimated by

$$\text{signal variance} = (\text{measured variance}) / (1 + \text{estimated percent error}). \quad (27)$$

Once the signal variance is estimated, an estimate of  $D/r_0$  is found using Eqn. (24). Results are shown in Fig. 28. As expected, the first variance based method is the best once a sufficient number of frames have been averaged. However, this optimized solution represents an idealized case where perfect knowledge of the noise statistics is assumed. Once the information available to the statistical model is reduced, as in the cases of the “level playing field” and “best guess” solutions, we see that the performance of the neural network is comparable if not better. The neural network is clearly better than the best guess solution. In the case of the level playing field, performance is better or worse depending on the situation. If we must average the estimate over small numbers of frames (20 or less), then the neural network is the better choice. If, however, we average over more than 20 frames, then the variance based method is the better choice.

To further investigate  $D/r_0$  estimation, the above test is repeated on tilt removed data. This test simulates an adaptive optics systems that removes the global tilt across the pupil before processing the incident, aberrated wavefront. The range of parameters is the same ( $D/r_0$  between 5 and 20, with error level of 0-25%), and the same three variance based estimators are compared to the performance of a neural network. In this case a neural network of 120 hidden nodes is trained to estimate  $D/r_0$ . The results are shown in Fig. 29. These results are similar those shown in Fig. 28. These results also show that all methods of  $D/r_0$  estimation performed better on global tilt removed data than on data with global tilt. This is due to the change in the covariance matrix of the data once global tilt is removed. When global tilt is removed, the variance of the individual elements decreases. Also, the relative magnitude of the off diagonal elements in the covariance matrix decreases. This reduction has the effect of making the individual slope measurements more independent

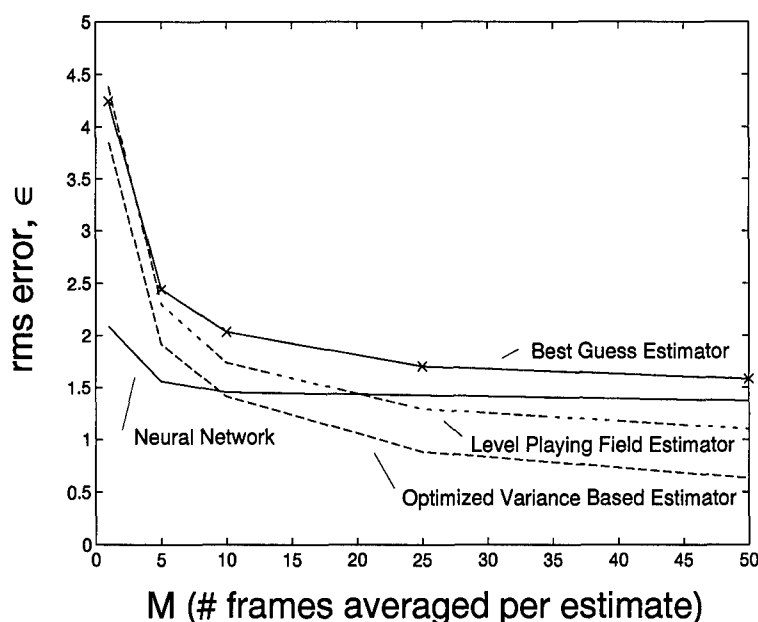


Figure 28. Comparison of the neural network and variance based estimation of  $D/r_0$  with WFS slope measurement error present. RMS error plotted versus  $M$ , the number of frames averaged per  $D/r_0$  value. The RMS error is averaged over 1000 randomly selected values of  $D/r_0$ . WFS mean square slope measurement error is 0-25%.

from the other measurements within a frame. Therefore, each frame of data has a better chance of being representative of the expected data statistics, and thus yields a better  $D/r_0$  estimate.

As a final test of neural networks, 256 frames of real data from the Starfire Optical Range, Phillips Laboratory, Kirtland AFB, New Mexico are tested. The data came from the 1.5m telescope with the WFS configuration found in Reference [5]. Four independent sets of  $5 \times 5$  arrays of slope measurements were extracted from each frame of data. The Starfire Optical Range estimated that  $D/r_0$  was 5.85 and noise conditions were low at the time the data were taken. A neural network with 80 hidden nodes and a sigmoid output node is trained on data with  $D/r_0$  in the range of 2.0-9.0, and WFS slope estimation error in the range of 0-25% of the slope signal variance. The neural network is then tested with the real telescope data. The average  $D/r_0$  estimate is 5.76, with a variance of 0.78. This

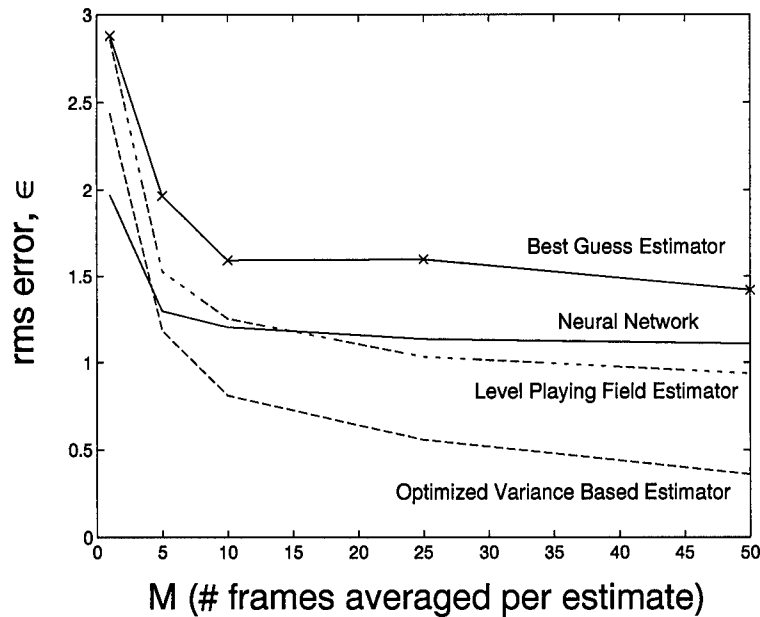


Figure 29. Comparison of the neural network and variance based estimation of  $D/r_0$  on global tilt removed data with WFS slope measurement error present. RMS error plotted versus  $M$ , the number of frames averaged per  $D/r_0$  value. The RMS error is averaged over 1000 randomly selected values of  $D/r_0$ . WFS mean square slope measurement error is 0-25%.

shows that techniques trained on computer generated data can operate on “real world” data.

Overall, several conclusions can be drawn about estimating  $D/r_0$ . First, the removal of global tilt as is often done in adaptive optics systems improves the performance of all the methods tested. Second, if timely, accurate knowledge of WFS slope estimation error level is available, then the statistical methods will, in general, outperform the neural network. Finally, if  $D/r_0$  is believed to be changing at a relatively fast rate, the neural network outperforms all conventional methods when the  $D/r_0$  estimate is averaged over small numbers of frames.

#### 4.2 Estimation of the Wind Speed Profile

Having knowledge of the wind speed profile would allow optimized wavefront reconstruction algorithms to compensate for the system time delay. The effect of changing wind speeds is to change the covariances between slope measurements at different times. Because each wind speed profile yields a unique off-diagonal structure to the covariance matrix, a statistics based wind speed profile estimator is not available. However, neural networks are tested to see if wind speed estimation is possible. Tests are conducted on 4 layer, and 2 layer (compressed 4 layer with first layer equal to strength of layers 1 and 2 of the 4 layer model, and the second layer equal to the strength of layers 3 and 4) atmospheric models. Tests with 2, 4, and 6 frames of slope measurements as inputs are conducted. Only in the most benign case of a 2 layer model, 6 frames of input,  $D/r_0 = 1.0$ , no WFS slope measurement error, and wind speeds between  $\pm 0.25D$  per frame, are acceptable results found. In this case, neural networks are able to estimate the lower layer (about 96% of the overall turbulence strength)  $x$  and  $y$  wind speeds with a MSE of  $0.0028D$ , and the upper layer wind speeds with a MSE of  $0.0056D$ . While these results are good, neural networks are not able to estimate wind speeds with any degree of accuracy once  $D/r_0$  is allowed to vary, or WFS slope estimation error is added to the data. Even with an accurate estimate of the covariance matrix which defines the temporal slope data, extraction of the wind speed profile would not be possible. Because many wind speeds are integrated in order to generate a single temporal slope covariance matrix (see Eqn. (6)), reversing the process to obtain the wind speeds from the single covariance matrix will not work. Therefore, it is determined that estimating wind speeds from the WFS slope measurements of a single beacon is not a viable option.

#### 4.3 Estimation of the Relative Atmospheric Layer Strengths

Knowledge of the relative atmospheric layer strengths would allow optimized wavefront reconstruction algorithms to compensate for system time delays or anisoplanatic effects. However, just like wind speeds, the effect of changing layer strengths is to change the

covariances between slope measurements at different times. Therefore, a statistics based relative layer strength estimator is not available. Neural networks also fail to perform this task with any accuracy. In the most benign case of estimates based on 6 frames of slope measurements, fixed wind speeds,  $D/r_0 = 1.0$ , no WFS slope measurement error, and a 2 layer atmospheric model where the lower layer ranges from 70-100% of strength, and the upper layer holds the remainder, estimation errors are extremely large. Again, just like estimating the wind speed profile, the fact that many layer strengths are integrated to generate a single temporal slope covariance matrix (see Eqn. (6)), reversing the process to obtain the layer strengths from the single covariance matrix will not work. Therefore, it is determined that estimating the relative atmospheric layer strengths from the WFS slope measurements of a single beacon is not a viable option.

#### *4.4 Estimation of WFS Mean Square Slope Estimation Error*

Another key parameter is the WFS mean square slope measurement error. The earlier results of the measurement error reduction tests in Section 3.1.1 indicate that a Bayes solution, optimized for a single  $D/r_0$  value (12.5) and a single slope measurement error level (12.5%), is able to outperform a neural network solution. The results also show that the closer the measurement error variance used in the Bayes solution is to the true measurement error level, the better the performance achieved. Therefore, tests are conducted to estimate the variance of the measurement error as a fraction (or percent) of signal variance. Slope vectors from a  $5 \times 5$  array of subapertures are generated to train a neural network.  $D/r_0$  is uniformly distributed over a range of 5-20, or 1 to 4  $r_0$ 's per subaperture. The measurement error level is uniformly distributed over a range of 0-100%, yielding a SNR 1 and greater. A neural network is trained to take as inputs 50 WFS measurements of a single frame and estimate the ratio of measurement error variance to signal variance. The neural network has 60 hidden layer nodes, and a sigmoid output node. For comparison, a conventional method based on the sample based variance of the data is used. This method is very similar to the variance based method used to estimate  $D/r_0$

(described in Section 4.1). For this variance based method,  $D/r_0$  is assumed to be known, and thus the variance of the slope signal can be subtracted. This leaves an estimate of measurement error variance. Since the signal variance is dependent on  $D/r_0$ , and  $D/r_0$  is assumed to be known, we can then calculate the measurement error to signal variance ratio. The neural network and variance based method are then tested with independent test data. Test data are generated over the entire range of  $D/r_0$  and measurement error levels. For each of 1000 randomly selected  $D/r_0$  and measurement error levels,  $M$  random realizations of WFS measurements are generated. Then, the neural network and the variance based estimator average their estimate of the measurement error level over the  $M$  realizations. The MSE between the 1000 average estimates and their true values is measured. As in  $D/r_0$  estimation, the network is compared to three forms of the variance based method. The first assumes perfect knowledge of  $D/r_0$  and thus represents the best variance based estimator. For the second method, the variance calculations are made assuming a nominal value of  $D/r_0 = 12.5$ , thus creating a level playing field. Finally, the third method takes into account a best guess of  $D/r_0$  that could be produced using the best guess variance based estimator described in Section 4.1. This  $D/r_0$  estimator has a MSE of 1.21. Therefore, the estimate of  $D/r_0$  is allowed to vary normally about the true value with a variance of 1.21. The results of all four methods are shown in Fig. 30.

Figure 30 shows that the optimized variance based estimator outperforms the neural network. While the errors obtained using the network are lower than the variance based estimator when small numbers of frames are averaged, the performance of the variance based estimator exceeds that of the neural network at  $\approx 20$  frames of averaging. However, the neural network does outperform both the “level playing field” and the “best guess” variance based estimators.

Again, a neural network of 80 hidden nodes is trained to estimate measurement error levels for global tilt removed data. Global tilt removed data is generated over the same ranges of parameters, ( $D/r_0$  between 5-20, with measurement error variance between 0-100%). The neural networks performance is compared to all three forms of variance based

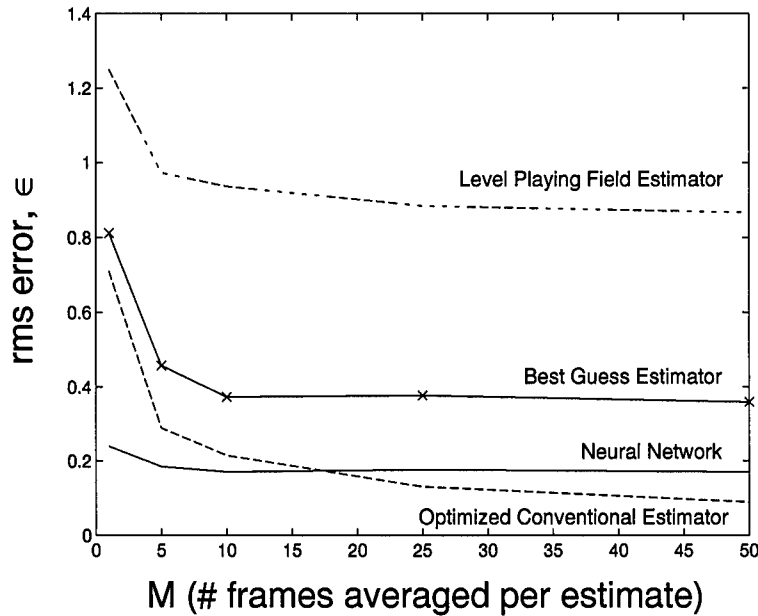


Figure 30. Comparison of neural network and variance based estimators for WFS slope measurement error estimation. RMS error plotted versus  $M$ , the number of frames averaged per error level. The RMS error is averaged over 1000 randomly selected error levels. Error level from 0-100% for  $D/r_0$  between 5-20.

estimator. The results are shown in Fig. 31. Again, the first variance based method performs best, and the neural network performs better than both the “level playing field” and “best guess” variance based methods.

Overall, the neural network performs better than the statistics based estimator for estimating the WFS mean square slope estimation error. While the optimized statistical estimator performs best, it requires perfect knowledge of other key parameters which are not always available. Also, the neural network does perform better than the optimized statistical estimator when the estimate is averaged over small numbers of frames. Finally, the removal of global tilt improves the performance of all the slope estimation error estimators tested.

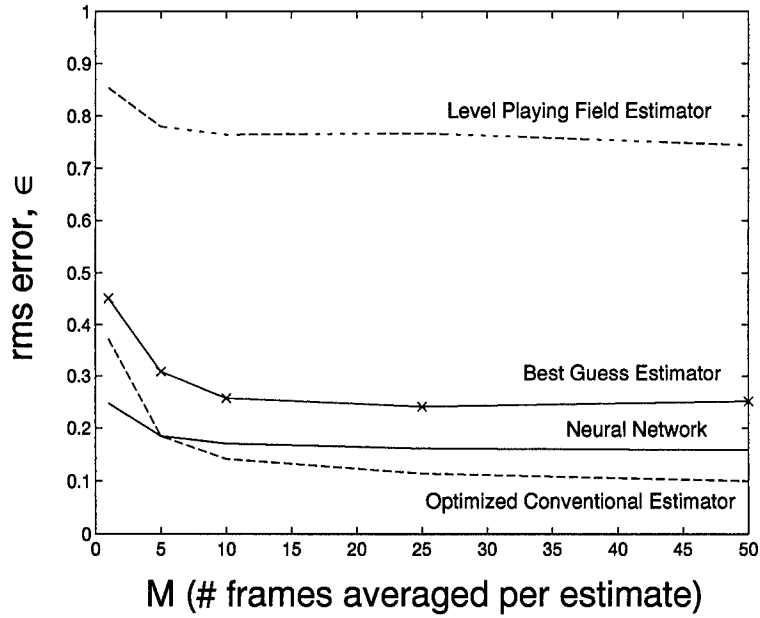


Figure 31. Comparison of neural network and variance based estimators for WFS slope measurement error estimation on data with global tilt removed. RMS error plotted versus  $M$ , the number of frames averaged per error level. The RMS error is averaged over 1000 randomly selected error levels. Error level from 0-100% for  $D/r_0$  between 5-20.

#### 4.5 Key Parameter Estimation Summary

Overall we find that some key parameter estimation is viable. Both neural networks and statistical estimators perform well when the parameters estimated do not affect the off-diagonal structure of the slope covariance matrix. These parameters include  $D/r_0$ , which only scales the entire covariance matrix, and the WFS mean square slope estimation error, which only changes the diagonal elements of the covariance matrix. For these parameters, we find that statistical estimators perform better in estimating  $D/r_0$ , while neural networks are best at estimating the WFS slope estimation error. However, when estimates are based on averaging over small numbers of frames, neural networks are better in both cases. For those parameters which do affect the relative structure of the off-diagonal elements of the slope covariance matrix, we find that estimation of the parameter from the WFS slope measurements is not a viable option. These parameters include the wind speed profile, and

the relative atmospheric layer strengths. Also, for those parameters which can be estimated from the WFS slope measurements, the removal of global tilt improves the estimate.

## V. Conclusions

This research investigated the appropriateness of processing WFS slope measurements to improve adaptive optics performance. In order to conduct this research, new atmospheric models had to be developed which produced both slope and phase data with the proper spatial and temporal information. Both linear (statistical) and nonlinear (artificial neural network) methods were applied to improve the accuracy of WFS slope measurements and to estimate key atmospheric and system parameters. This chapter summarizes the results of the individual experiments performed throughout this research, then addresses the issues contained in the overall research goals.

### 5.1 Individual Experiment Summaries

Through the course of this research, individual experiments were conducted in improving the accuracy of WFS slope measurements and key parameter estimation. Both neural networks and statistics based methods were investigated and the results are compared to determine which methods provided the best performance. Experiments in improving the accuracy of WFS slope measurements included reducing the WFS mean square slope estimation error, both through the processing of a single frame of WFS slope measurements and improving the centroid estimation within a single WFS subaperture, and compensating for system time delay through temporal slope prediction. Experiments in key parameter estimation included estimating  $r_0$ , the atmospheric wind speed profile, the strengths of the atmospheric turbulence layers, and estimating the WFS mean square slope measurement error. These experiments are significant because they had not been previously investigated, and thus represent new work. Because adaptive optics correction is based on the measured slope signals, any effort which makes them more accurately match the true slope signals at the time of correction would improve the performance of the adaptive optics systems. The ability to maintain timely, accurate estimates of the key parameters would enable wavefront

reconstruction algorithms to operate in a more “optimal” fashion. Brief summaries of each of the experiments follow.

*5.1.1 Reducing WFS Mean Square Slope Estimation Error Through Processing a Frame of WFS Slope Measurements.* In the experiments which reduce the WFS mean square slope estimation error through the processing of an entire frame of WFS slope measurements, we find that both the neural network and the statistical solution perform well in both fixed seeing conditions, and when seeing conditions are allowed to vary. However, as long as a reasonable estimate of the system mean square slope measurement error exists, the statistical solution is the better choice. Also, it is shown that a neural network will approximate the optimized statistical solution when seeing conditions are fixed.

*5.1.2 Reducing WFS Mean Square Slope Estimation Error Through Improving the Centroid Estimation Within a Single WFS Subaperture.* In the experiments which reduce the slope measurement error within a single WFS subaperture, the neural network is clearly the better than the standard centroid estimator. While both methods show a nonlinear response in estimation, the neural networks provide more accurate estimates, over a larger dynamic range, and with less estimate variance.

*5.1.3 Compensating for System Time Delay.* In the experiments in improving WFS slope measurements accuracy through temporal slope prediction, we find that when seeing conditions are set, a neural network solution will approximate an optimized statistical solution. We find that a single neural network can be trained to perform under a broad range of seeing conditions, and that a single fixed statistical solution cannot provide benefit under those same conditions. Also, we see that prediction with a neural network can allow adaptive optics to function under a larger set of wind speeds than a system without prediction. We also find that temporal prediction can be applied to the problem of anisoplanatism, and we expect similar results in performance. Overall, neural networks

offer a viable solution for prediction of WFS slope measurements which helps compensate for system time delay.

*5.1.4 Estimating  $r_0$ .* In the experiments in estimating  $r_0$  from the WFS slope measurements, we find that both neural networks and statistical estimators can be used. If timely, accurate knowledge of WFS slope estimation error level is available, then the statistical methods will, in general, outperform the neural network. However, if  $r_0$  is believed to be changing at a relatively fast rate, the neural network outperforms all conventional methods when the  $r_0$  estimate is averaged over small numbers of frames.

*5.1.5 Estimating the Wind Speed Profile.* In the experiments in estimating  $r_0$  from the WFS slope measurements, we find that neural networks are not able to estimate wind speeds with any degree of accuracy once  $D/r_0$  is allowed to vary, or WFS slope estimation error is added to the data. Overall, it is determined that estimating wind speeds from the WFS slope measurements of a single beacon is not a viable option.

*5.1.6 Estimating the Strengths of the Atmospheric Turbulence Layers.* In the experiments in estimating  $r_0$  from the WFS slope measurements, we find that estimating the relative atmospheric layer strengths from the WFS slope measurements of a single beacon is not a viable option.

*5.1.7 Estimating the WFS Mean Square Slope Estimation Error.* Finally, in the experiments in estimating the WFS mean square slope estimation error from the WFS slope measurements, we find that the neural network performs better than the statistics based estimator for estimating the WFS mean square slope estimation error. While the optimized statistical estimator performs best, it requires perfect knowledge of other key parameters which are not always available. Also, the neural network does perform better than the optimized statistical estimator when the estimate is averaged over small numbers of frames.

## 5.2 *Conclusions on Overall Research Goals*

While the individual experiments in improving the accuracy of WFS slope measurements and key parameter estimation represent new work in the adaptive optics field with significant results, they also yield some broad conclusions about processing WFS slope measurements to improve adaptive optics performance. These conclusions should help direct and limit the scope of future efforts dealing with the processing of WFS slope measurements. Conclusions are drawn from the experiments on the following key issues:

1. What kinds of useful information can be extracted from the WFS slope measurements?
2. Which methods work best (statistical models or artificial neural networks)?
3. Can methods be developed which operate over useful ranges of seeing conditions?

The first issue deals with what can we reasonably expect to extract from the WFS slope measurements. As was stated earlier, many factors effect the statistics which ultimately govern the atmospheric abberations and the limits on adaptive optics system performance. These factors include  $r_0$ , the wind speed profile, and the strengths of the atmospheric turbulence layers. Also, the WFS mean square slope estimation effects the statistics of the measured slope signals. All these parameters effect the statistics of the measured slope signals by either changing the diagonal structure of the slope covariance matrix, by changing the off-diagonal structure of the slope covariance matrix, or by merely scaling the entire slope covariance matrix. How a particular parameter effects the slope covariance matrix plays a big role in our ability to accurately estimate that parameter from the measured slope signals.

Clearly all the experiments in improving the accuracy of WFS slope measurements, along with the experiments in estimating the key parameters of  $r_0$  and the WFS mean square slope estimation error were successful. These successes, along with the failures in estimating the atmospheric wind speed profile and the strength of the atmospheric turbulence layers yield significant insight into what kinds of processing of WFS slope signals

will be successful. In the area of improving the accuracy of WFS slope measurements through the processing of the slope measurements (as in reducing the WFS mean square slope estimation error and temporal slope prediction), if a statistical method can be found which minimizes the mean square error when seeing conditions are fixed, then the task should be able to be accomplished when seeing conditions are variable. However, the variable seeing conditions solution will not perform as well as an optimized solution. In the area of parameter estimation, we find that parameters which affect only the diagonal of the slope covariance matrix, or merely scale the entire slope covariance matrix can be accurately estimated. However, those parameters which change the off-diagonal structure of the slope covariance matrix, and thus information about those parameters is deeply embedded in the covariance statistics, are not easily estimated.

The second issue deals with choosing the proper method for extracting information from WFS slope measurements. This research compares the performance of statistics based methods with artificial neural networks. First we find that neural networks can approximate optimized statistical solutions when seeing conditions are fixed. This was shown in the experiments to reduce the WFS mean square slope estimation error through the processing of a single frame of slope measurements, and in the slope temporal prediction experiments. While the ability of neural networks to approximate optimized statistical methods had been proven in theory, it had not, before this research, been shown in application for non-classification problems. Next, we find that while both neural networks and statistical methods can function under variable seeing conditions, the neural networks tend to be more robust than the statistical methods. For statistical solutions, the more variables that effect the overall statistical solution, the less robust it becomes. However, the neural networks seem to maintain their robustness even when many variables govern the data. We also find that the neural network solutions are able to give good estimates of key parameters without having to average the estimate over many frames of slope data. The statistical estimators, however, only function well when the estimate can be averaged over large numbers of slope frames. Also, we see from the parameter estimation tests and the

test in reducing WFS measurement error within a single subaperture that neural networks operate much better than statistical solutions in the presence of noise when only a single frame of data is processed. This ability to operate in noisy conditions can be critical to system performance. Finally, we find that the removal of global tilt from the slope signal helps both the statistics based solutions and the neural networks in most cases. The only experiment where performance was not improved involved the reducing of the WFS slope estimation error through the processing of a single frame of slope measurements. Because tilt removal makes the individual slope measurements within a frame more independent, valuable information used in error reduction is lost when global tilt is removed. However, the impact of tilt removal on WFS slope measurement error reduction was small.

The final issue deals with developing flexible solution to improving adaptive optics performance. Because seeing conditions rarely remain fixed for any significant period of time, viable solutions for improving adaptive optics performance must be able to operate over wide ranges of seeing conditions. The experiments in this research indicate that viable solutions can be developed that operate over broad ranges of seeing conditions. While being developed to operate under variable seeing conditions, these solutions still provide significant performance in improving the accuracy of WFS slope measurements and in estimating key atmospheric and system parameters.

Overall, we find that the WFS slope measurements do contain useful information that can be extracted through various techniques. Simple transformations (either by neural network or statistical solution) on slope measurements can yield significant improvements in system accuracy without major changes to the adaptive optics system. In the areas of WFS measurement error reduction, temporal slope prediction, and parameter estimation, significant performance increases can be realized either directly through processing of the WFS slope measurements, or by using parameter estimates from the WFS slope measurements to increase the performance of wavefront reconstruction algorithms. Also, we find that both neural networks and statistical methods perform well when seeing conditions are

fixed, however neural networks are much more robust when operating under variable seeing conditions than are the statistical solutions.

## Appendix A. Development of Slope Covariance

This appendix provides a detailed development of the governing equation of the space-time slope screen covariance matrix. All of this work begins with the following equation developed by Ellerbroek [3]:

$$\begin{aligned}
 E[u_i u_j] = & 0.00969 \left( \frac{2\pi}{\lambda} \right)^2 \iint d\vec{x}_1 d\vec{x}_2 v_i(\vec{x}_1) v_j(\vec{x}_2) \\
 & \times \iint d\tau_1 d\tau_2 w_i(\tau_1) w_j(\tau_2) \sum_{j=1}^N C_n^2(z_j) \Delta z \\
 & \times \left\{ \int d\vec{k} |\vec{k}|^{-\frac{11}{3}} e^{(-j2\pi\vec{k} \cdot (\vec{x}_1 - \vec{x}_2))} e^{(-j2\pi(\tau_1 - \tau_2)\vec{k} \cdot \vec{v}(z_j))} + c \right\}, \quad (28)
 \end{aligned}$$

where  $u_i$  and  $u_j$  are either wavefront slopes or phases. For piston removed data

$$w_k(\tau) = \delta(t_k - \tau) \quad (29)$$

$$v_k(\vec{x}) = \begin{cases} W(\vec{x}) [\delta(\vec{x}_k - \vec{x}) - 1] & \text{for phase measurements} \\ w_i^s(\vec{x}) & \text{for slope measurements} \end{cases} \quad (30)$$

where  $t_k$  is the time of measurement  $u_k$ ,  $W(\vec{x})$  is the aperture function,  $\vec{x}_k$  is the position in the aperture of phase measurement  $u_k$ , and  $w_i^s(\vec{x})$  designates the gradient of the  $i$ th WFS subaperture weighting function. Starting with Eqn. (28), the following expression for the covariance,  $C_s$ , between any two slope measurements  $s_i(t_1)$  and  $s_j(t_2)$  at times  $t_1$  and  $t_2$  can be written:

$$\begin{aligned}
C_s(s_i(t_1), s_j(t_2)) &= E[s_i(t_1)s_j(t_2)] \\
&= 0.00969 \left(\frac{2\pi}{\lambda}\right)^2 \iint d\vec{x}_1 d\vec{x}_2 w_i^s(\vec{x}_1) w_j^s(\vec{x}_2) \\
&\quad \times \int \int d\tau_1 d\tau_2 \delta(\tau_1 - t_1) \delta(\tau_2 - t_2) \sum_{j=1}^N C_n^2(z_j) \Delta z \\
&\quad \times \left\{ \int d\vec{k} |\vec{k}|^{-\frac{11}{3}} e^{(-j2\pi\vec{k}\cdot(\vec{x}_1-\vec{x}_2))} e^{(-j2\pi(\tau_1-\tau_2)\vec{k}\cdot\vec{v}(z_j))} + c \right\}.
\end{aligned} \tag{31}$$

Letting  $k = |\vec{k}|$ ,  $\vec{\beta} = 2\pi(\vec{x}_1 - \vec{x}_2 + (t_1 - t_2)\vec{v}(z_j))$ , and integrating over both  $\tau_1$  and  $\tau_2$  yields

$$\begin{aligned}
C_s(s_i(t_1), s_j(t_2)) &= 0.00969 \left(\frac{2\pi}{\lambda}\right)^2 \iint d\vec{x}_1 d\vec{x}_2 w_i^s(\vec{x}_1) w_j^s(\vec{x}_2) \sum_{j=1}^N C_n^2(z_j) \Delta z \\
&\quad \times \left\{ \int d\vec{k} k^{-\frac{11}{3}} e^{(-j\vec{k}\cdot\vec{\beta})} + c \right\}.
\end{aligned} \tag{32}$$

However,

$$\vec{k} \cdot \vec{\beta} = k\beta \cos \theta, \tag{33}$$

where  $\beta = |\vec{\beta}|$  and

$$d\vec{k} = k dk d\theta. \tag{34}$$

Substitution yields

$$\begin{aligned}
C_s(s_i(t_1), s_j(t_2)) &= 0.00969 \left(\frac{2\pi}{\lambda}\right)^2 \iint d\vec{x}_1 d\vec{x}_2 w_i^s(\vec{x}_1) w_j^s(\vec{x}_2) \sum_{j=1}^N C_n^2(z_j) \Delta z \\
&\quad \times \left\{ \int d\theta \int dk k^{-\frac{8}{3}} e^{(-jk\beta \cos \theta)} + c \right\}.
\end{aligned} \tag{35}$$

Using the following relationship

$$\int_0^{2\pi} e^{-ja \cos(\theta-\phi)} d\theta = 2\pi J_0(a), \quad (36)$$

yields

$$\begin{aligned} C_s(s_i(t_1), s_j(t_2)) &= (2\pi)(0.00969) \left(\frac{2\pi}{\lambda}\right)^2 \iint d\vec{x}_1 d\vec{x}_2 w_i^s(\vec{x}_1) w_j^s(\vec{x}_2) \sum_{j=1}^N C_n^2(z_j) \Delta z \\ &\times \left\{ \int dk k^{-\frac{8}{3}} J_0(k\beta) + c \right\}. \end{aligned} \quad (37)$$

Now, any value can be chosen for  $c$  as long as it is independent of position  $\vec{x}$ . Therefore, choose  $c = -k^{-\frac{8}{3}}$ . Then

$$\begin{aligned} C_s(s_i(t_1), s_j(t_2)) &= -(2\pi)(0.00969) \left(\frac{2\pi}{\lambda}\right)^2 \iint d\vec{x}_1 d\vec{x}_2 w_i^s(\vec{x}_1) w_j^s(\vec{x}_2) \sum_{j=1}^N C_n^2(z_j) \Delta z \\ &\times \int dk [1 - J_0(k\beta)] k^{-\frac{8}{3}}. \end{aligned} \quad (38)$$

Multiplying the equation by  $\left(\frac{\beta}{\beta}\right)^{\frac{8}{3}}$  yields

$$\begin{aligned} C_s(s_i(t_1), s_j(t_2)) &= -(2\pi)(0.00969) \left(\frac{2\pi}{\lambda}\right)^2 \iint d\vec{x}_1 d\vec{x}_2 w_i^s(\vec{x}_1) w_j^s(\vec{x}_2) \sum_{j=1}^N C_n^2(z_j) \Delta z \\ &\times \int dk \beta^{\frac{8}{3}} [1 - J_0(k\beta)] (k\beta)^{-\frac{8}{3}}. \end{aligned} \quad (39)$$

Using the identity

$$\int [1 - J_0(x)] x^{-p} dx = \pi \left\{ 2^p \Gamma^2\left(\frac{p+1}{2}\right) \sin \left[ \frac{\pi(p-1)}{2} \right] \right\}^{-1}, \quad (40)$$

when

$$1 < p < 3, \quad (41)$$

yields

$$\begin{aligned} C_s(s_i(t_1), s_j(t_2)) &= -(2\pi)(0.00969) \left(\frac{2\pi}{\lambda}\right)^2 \iint d\vec{x}_1 d\vec{x}_2 w_i^s(\vec{x}_1) w_j^s(\vec{x}_2) \sum_{j=1}^N C_n^2(z_j) \Delta z \\ &\quad \times \beta^{\frac{5}{3}} \pi \left\{ 2^{\frac{8}{3}} \Gamma^2\left(\frac{11}{6}\right) \sin\left[\frac{\pi(5)}{6}\right] \right\}^{-1}, \end{aligned} \quad (42)$$

$$C_s(s_i(t_1), s_j(t_2)) = -(0.068) \left(\frac{2\pi}{\lambda}\right)^2 \iint d\vec{x}_1 d\vec{x}_2 w_i^s(\vec{x}_1) w_j^s(\vec{x}_2) \sum_{j=1}^N C_n^2(z_j) \Delta z \beta^{\frac{5}{3}}, \quad (43)$$

Substituting back in for  $\beta$  yields

$$\begin{aligned} C_s(s_i(t_1), s_j(t_2)) &= -(0.068) \left(\frac{2\pi}{\lambda}\right)^2 \sum_{j=1}^N C_n^2(z_j) \Delta z \\ &\quad \times \iint d\vec{x}_1 d\vec{x}_2 w_i^s(\vec{x}_1) w_j^s(\vec{x}_2) (2\pi |\vec{x}_1 - \vec{x}_2 + (t_1 - t_2)\vec{v}(z_j)|)^{\frac{5}{3}}. \end{aligned} \quad (44)$$

Finally, substituting

$$C_n^2(z_j) \Delta z = \frac{6.88}{2.91 \left(\frac{2\pi}{\lambda}\right)^2} r_0(z_j)^{-\frac{5}{3}}, \quad (45)$$

normalizing the aperture by its dimension  $l$ , and letting

$$f(z_j) = \left(\frac{r_0}{r_0(z_j)}\right)^{\frac{5}{3}}, \quad (46)$$

where  $f(z_j)$  equals the fraction of all turbulence in the  $j$ th layer at altitude  $z_j$  yields

$$\begin{aligned}
C_s(s_i(t_1), s_j(t_2)) &= E[s_i(t_1)s_j(t_2)] \\
&= -3.44 \left(\frac{D}{r_0}\right)^{\frac{5}{3}} \sum_{k=1}^N f(z_k) \\
&\quad \times \int \int d\vec{x}_1 d\vec{x}_2 w_i^s(\vec{x}_1) w_j^s(\vec{x}_2) | \vec{x}_1 - \vec{x}_2 - (t_1 - t_2)\vec{v}(z_k) |^{\frac{5}{3}}. \quad (47)
\end{aligned}$$

## Appendix B. Development of Phase Covariance

This appendix provides a detailed development of the governing equation of the space-time phase screen covariance matrix. All of this work begins with Eqn. (28) developed by Ellerbroek [3]. Starting with Eqn. (28), the following expression for the covariance,  $C_p$ , between any two phase measurements  $\phi(\vec{x}_1, t_1)$  and  $\phi(\vec{x}_2, t_2)$  at locations  $\vec{x}_1$  and  $\vec{x}_2$  and times  $t_1$  and  $t_2$  can be written:

$$C_p(\vec{x}_1, t_1, \vec{x}_2, t_2) = E[\phi(\vec{x}_1, t_1)\phi(\vec{x}_2, t_2)] \quad (48)$$

$$\begin{aligned} &= 0.00969 \left(\frac{2\pi}{\lambda}\right)^2 \iint d\vec{\eta} d\vec{\xi} \\ &\quad \times W(\vec{\eta}) [\delta(\vec{\eta} - \vec{x}_1) - f(\vec{\eta})f(\vec{x}_1)] W(\vec{\xi}) [\delta(\vec{\xi} - \vec{x}_2) - f(\vec{\xi})f(\vec{x}_2)] \\ &\quad \times \int \int d\tau_1 d\tau_2 \delta(\tau_1 - t_1) \delta(\tau_2 - t_2) \sum_{j=1}^N C_n^2(z_j) \Delta z \\ &\quad \times \left\{ \int d\vec{k} \left| \vec{k} \right|^{-\frac{11}{3}} e^{(-j2\pi\vec{k} \cdot (\vec{\eta} - \vec{\xi}))} e^{(-j2\pi(\tau_1 - \tau_2)\vec{k} \cdot \vec{v}(z_j))} + c \right\}, \end{aligned} \quad (49)$$

where  $W(\vec{\alpha})$  is the aperture function,  $C_n^2(z_j)$  is the structure constant of the  $j$ th layer at altitude  $z_j$ ,  $\vec{v}(z_j)$  is the velocity of the  $j$ th layer at altitude  $z_j$ , and for piston removal  $f(\vec{x}) = 1$ . Substitution for  $f(\vec{x})$  and integration over both  $\tau_1$  and  $\tau_2$  yields

$$\begin{aligned} C_p(\vec{x}_1, t_1, \vec{x}_2, t_2) &= 0.00969 \left(\frac{2\pi}{\lambda}\right)^2 \iint d\vec{\eta} d\vec{\xi} \\ &\quad \times W(\vec{\eta}) [\delta(\vec{\eta} - \vec{x}_1) - 1] W(\vec{\xi}) [\delta(\vec{\xi} - \vec{x}_2) - 1] \sum_{j=1}^N C_n^2(z_j) \Delta z \\ &\quad \times \left\{ \int d\vec{k} \left| \vec{k} \right|^{-\frac{11}{3}} e^{(-j2\pi[\vec{k} \cdot (\vec{\eta} - \vec{\xi} + (t_1 - t_2)\vec{v}(z_j))])} + c \right\}. \end{aligned} \quad (50)$$

Since we are not interested in time sequenced phase screens, the time dependence and layer dependence can be removed. Also,

$$\vec{k} \cdot (\vec{\eta} - \vec{\xi}) = |\vec{k}| |\vec{\eta} - \vec{\xi}| \cos \theta \quad (51)$$

when

$$d\vec{k} = |\vec{k}| d|\vec{k}| d\theta. \quad (52)$$

Substitution of Eqns. (51) and (52) into Eqn. (50) yields

$$\begin{aligned} C_p(\vec{x}_1, \vec{x}_2) &= 0.00969 \left( \frac{2\pi}{\lambda} \right)^2 \iint d\vec{\eta} d\vec{\xi} \\ &\times W(\vec{\eta}) [\delta(\vec{\eta} - \vec{x}_1) - 1] W(\vec{\xi}) [\delta(\vec{\xi} - \vec{x}_2) - 1] C_n^2 \\ &\times \left\{ \int d\theta \int d|\vec{k}| |\vec{k}|^{-\frac{8}{3}} e^{(-j2\pi[|\vec{k}||\vec{\eta}-\vec{\xi}|\cos\theta])} + c \right\}, \end{aligned} \quad (53)$$

where  $C_n^2$  is the effective structure constant for the entire atmosphere. Using the following relationship

$$\int_0^{2\pi} e^{-ja\cos(\theta-\phi)} d\theta = 2\pi J_0(a), \quad (54)$$

yields

$$\begin{aligned} C_p(\vec{x}_1, \vec{x}_2) &= (2\pi)(0.00969) \left( \frac{2\pi}{\lambda} \right)^2 \iint d\vec{\eta} d\vec{\xi} \\ &\times W(\vec{\eta}) [\delta(\vec{\eta} - \vec{x}_1) - 1] W(\vec{\xi}) [\delta(\vec{\xi} - \vec{x}_2) - 1] C_n^2 \\ &\times \left\{ \int d|\vec{k}| |\vec{k}|^{-\frac{8}{3}} J_0(2\pi |\vec{k}| |\vec{\eta} - \vec{\xi}|) + c \right\}. \end{aligned} \quad (55)$$

Now, any value can be chosen for  $c$  as long as it is independent of position  $\vec{x}$ . Therefore, choose  $c = -|\vec{k}|^{-\frac{8}{3}}$ . Then

$$\begin{aligned} C_p(\vec{x}_1, \vec{x}_2) &= -(2\pi)(0.00969) \left( \frac{2\pi}{\lambda} \right)^2 \iint d\vec{\eta} d\vec{\xi} \\ &\times W(\vec{\eta}) [\delta(\vec{\eta} - \vec{x}_1) - 1] W(\vec{\xi}) [\delta(\vec{\xi} - \vec{x}_2) - 1] C_n^2 \\ &\times \int d|\vec{k}| |\vec{k}| \left[ 1 - J_0(2\pi |\vec{k}| |\vec{\eta} - \vec{\xi}|) \right] |\vec{k}|^{-\frac{8}{3}}. \end{aligned} \quad (56)$$

To keep things simple, let

$$\beta = 2\pi |\vec{\eta} - \vec{\xi}|, \quad (57)$$

and multiply the equation by  $\left(\frac{\beta}{\lambda}\right)^{\frac{8}{3}}$ . Then

$$\begin{aligned}
C_p(\vec{x}_1, \vec{x}_2) = & -(2\pi)(0.00969) \left(\frac{2\pi}{\lambda}\right)^2 \iint d\vec{\eta} d\vec{\xi} \\
& \times W(\vec{\eta}) [\delta(\vec{\eta} - \vec{x}_1) - 1] W(\vec{\xi}) [\delta(\vec{\xi} - \vec{x}_2) - 1] C_n^2 \\
& \times \int d|\vec{k}| \beta^{\frac{8}{3}} [1 - J_0(|\vec{k}| \beta)] (|\vec{k}| \beta)^{-\frac{8}{3}}.
\end{aligned} \tag{58}$$

Using the identity

$$\int [1 - J_0(x)] x^{-p} dx = \pi \left\{ 2^p \Gamma^2\left(\frac{p+1}{2}\right) \sin \left[ \frac{\pi(p-1)}{2} \right] \right\}^{-1}, \tag{59}$$

when

$$1 < p < 3, \tag{60}$$

yields

$$\begin{aligned}
C_p(\vec{x}_1, \vec{x}_2) = & -(2\pi)(0.00969) \left(\frac{2\pi}{\lambda}\right)^2 \iint d\vec{\eta} d\vec{\xi} \\
& \times W(\vec{\eta}) [\delta(\vec{\eta} - \vec{x}_1) - 1] W(\vec{\xi}) [\delta(\vec{\xi} - \vec{x}_2) - 1] C_n^2 \\
& \times \beta^{\frac{5}{3}} \pi \left\{ 2^{\frac{8}{3}} \Gamma^2\left(\frac{11}{6}\right) \sin \left[ \frac{\pi(5)}{6} \right] \right\}^{-1},
\end{aligned} \tag{61}$$

$$\begin{aligned}
= & -(0.068) \left(\frac{2\pi}{\lambda}\right)^2 \iint d\vec{\eta} d\vec{\xi} \\
& \times W(\vec{\eta}) [\delta(\vec{\eta} - \vec{x}_1) - 1] W(\vec{\xi}) [\delta(\vec{\xi} - \vec{x}_2) - 1] C_n^2 \beta^{\frac{5}{3}},
\end{aligned} \tag{62}$$

$$\begin{aligned}
= & -(0.068) \left(\frac{2\pi}{\lambda}\right)^2 C_n^2 \iint d\vec{\eta} d\vec{\xi} W(\vec{\eta}) W(\vec{\xi}) \beta^{\frac{5}{3}} \\
& \times [\delta(\vec{\eta} - \vec{x}_1) \delta(\vec{\xi} - \vec{x}_2) - \delta(\vec{\eta} - \vec{x}_1) - \delta(\vec{\xi} - \vec{x}_2) + 1],
\end{aligned} \tag{63}$$

$$\begin{aligned}
C_p(\vec{x}_1, \vec{x}_2) = & -(0.068) \left( \frac{2\pi}{\lambda} \right)^2 C_n^2 \\
& \times \left[ \int \int d\vec{\eta} d\vec{\xi} W(\vec{\eta}) W(\vec{\xi}) \beta^{\frac{5}{3}} \delta(\vec{\eta} - \vec{x}_1) \delta(\vec{\xi} - \vec{x}_2) \right. \\
& - \int \int d\vec{\eta} d\vec{\xi} W(\vec{\eta}) W(\vec{\xi}) \beta^{\frac{5}{3}} \delta(\vec{\eta} - \vec{x}_1) \\
& - \int \int d\vec{\eta} d\vec{\xi} W(\vec{\eta}) W(\vec{\xi}) \beta^{\frac{5}{3}} \delta(\vec{\xi} - \vec{x}_2) \\
& \left. + \int \int d\vec{\eta} d\vec{\xi} W(\vec{\eta}) W(\vec{\xi}) \beta^{\frac{5}{3}} \right]. \tag{64}
\end{aligned}$$

Substituting back in for  $\beta$  yields

$$\begin{aligned}
C_p(\vec{x}_1, \vec{x}_2) = & -(0.068) \left( \frac{2\pi}{\lambda} \right)^2 C_n^2 \\
& \times \left[ \int \int d\vec{\eta} d\vec{\xi} W(\vec{\eta}) W(\vec{\xi}) \left( 2\pi |\vec{\eta} - \vec{\xi}| \right)^{\frac{5}{3}} \delta(\vec{\eta} - \vec{x}_1) \delta(\vec{\xi} - \vec{x}_2) \right. \\
& - \int \int d\vec{\eta} d\vec{\xi} W(\vec{\eta}) W(\vec{\xi}) \left( 2\pi |\vec{\eta} - \vec{\xi}| \right)^{\frac{5}{3}} \delta(\vec{\eta} - \vec{x}_1) \\
& - \int \int d\vec{\eta} d\vec{\xi} W(\vec{\eta}) W(\vec{\xi}) \left( 2\pi |\vec{\eta} - \vec{\xi}| \right)^{\frac{5}{3}} \delta(\vec{\xi} - \vec{x}_2) \\
& \left. + \int \int d\vec{\eta} d\vec{\xi} W(\vec{\eta}) W(\vec{\xi}) \left( 2\pi |\vec{\eta} - \vec{\xi}| \right)^{\frac{5}{3}} \right]. \tag{65}
\end{aligned}$$

Taking advantage of integration over  $\delta$  functions yields

$$\begin{aligned}
C_p(\vec{x}_1, \vec{x}_2) = & -(0.068) \left( \frac{2\pi}{\lambda} \right)^2 C_n^2 \\
& \times \left[ W(\vec{\eta}) W(\vec{\xi}) (2\pi |\vec{x}_1 - \vec{x}_2|)^{\frac{5}{3}} \right. \\
& - \int d\vec{\xi} W(\vec{x}_1) W(\vec{\xi}) \left( 2\pi |\vec{x}_1 - \vec{\xi}| \right)^{\frac{5}{3}} \\
& - \int d\vec{\eta} W(\vec{\eta}) W(\vec{x}_2) (2\pi |\vec{\eta} - \vec{x}_2|)^{\frac{5}{3}} \\
& \left. + \int \int d\vec{\phi} d\vec{\theta} W(\vec{\phi}) W(\vec{\theta}) \left( 2\pi |\vec{\phi} - \vec{\theta}| \right)^{\frac{5}{3}} \right]. \tag{66}
\end{aligned}$$

Finally, substituting

$$C_n^2 = \frac{6.88}{2.91 \left(\frac{2\pi}{\lambda}\right)^2} r_0^{-\frac{5}{3}}, \quad (67)$$

and normalizing the aperture by its dimension  $L$  such that the aperture functions,  $W(\vec{\alpha})$ , range from  $-\frac{1}{2}$  to  $\frac{1}{2}$ , yields

$$\begin{aligned} C_p(\vec{x}_1, \vec{x}_2) = & -3.44 \left(\frac{L}{r_0}\right)^{\frac{5}{3}} \\ & \times \left[ W(\vec{\eta})W(\vec{\xi}) (|\vec{x}_1 - \vec{x}_2|)^{\frac{5}{3}} \right. \\ & - \int d\vec{\xi} W(\vec{x}_1)W(\vec{\xi}) (|\vec{x}_1 - \vec{\xi}|)^{\frac{5}{3}} \\ & - \int d\vec{\eta} W(\vec{\eta})W(\vec{x}_2) (|\vec{\eta} - \vec{x}_2|)^{\frac{5}{3}} \\ & \left. + \int \int d\vec{\phi} d\vec{\theta} W(\vec{\phi})W(\vec{\theta}) (|\vec{\phi} - \vec{\theta}|)^{\frac{5}{3}} \right]. \quad (68) \end{aligned}$$

### Appendix C. Phase covariance calculation: Gegenbauer polynomial technique

We begin with Eq. (13), the final form of the phase covariance for the Kolmogorov power spectrum.

$$\begin{aligned}
C_p(\vec{x}_1, t_1, \vec{x}_2, t_2) = & -3.44 \left( \frac{L}{r_0} \right)^{\frac{5}{3}} \sum_{j=1}^N f(z_j) \\
& \times \left[ W(\vec{\eta})W(\vec{\xi}) (|\vec{x}_1 - \vec{x}_2 + (t_1 - t_2)\vec{v}(z_j)|)^{\frac{5}{3}} \right. \\
& - \int d\vec{\xi} W(\vec{x}_1)W(\vec{\xi}) (|\vec{x}_1 - \vec{\xi} + (t_1 - t_2)\vec{v}(z_j)|)^{\frac{5}{3}} \\
& - \int d\vec{\eta} W(\vec{\eta})W(\vec{x}_2) (|\vec{\eta} - \vec{x}_2 + (t_1 - t_2)\vec{v}(z_j)|)^{\frac{5}{3}} \\
& \left. + \int d\vec{\phi} d\vec{\theta} W(\vec{\phi})W(\vec{\theta}) (|\vec{\phi} - \vec{\theta} + (t_1 - t_2)\vec{v}(z_j)|)^{\frac{5}{3}} \right]. \quad (69)
\end{aligned}$$

The Gegenbauer polynomial technique requires a circular aperture of unit radius [23], which we already have. Therefore, substituting in the Gegenbauer polynomial functions yields

$$\begin{aligned}
C_p(\vec{x}_1, t_1, \vec{x}_2, t_2) = & -3.44 \left( \frac{L}{r_0} \right)^{\frac{5}{3}} \sum_{j=1}^N f(z_j) \left\{ \begin{aligned} & |\vec{x}_1 - \vec{x}_2 + (t_1 - t_2)\vec{v}(z_j)|^{5/3} \\ & - F_1(-\vec{x}_1 + (t_1 - t_2)\vec{v}(z_j)) \\ & - F_1(\vec{x}_2 + (t_1 - t_2)\vec{v}(z_j)) \\ & + F_2((t_1 - t_2)\vec{v}(z_j)) \end{aligned} \right\}. \quad (70)
\end{aligned}$$

where

$$F_1(\vec{\Omega}) = \begin{cases} \frac{6}{11} {}_2F_1\left(\frac{-11}{6}, \frac{-5}{6}; 1; |\vec{\Omega}|^2\right) & |\vec{\Omega}| \leq 1 \\ |\vec{\Omega}|^{5/3} {}_2F_1\left(\frac{-5}{6}, \frac{-5}{6}; 2; |\vec{\Omega}|^{-2}\right) & |\vec{\Omega}| \geq 1 \end{cases} \quad (71)$$

$${}_2F_1(a, b; c; z) = \frac{\Gamma(c)}{\Gamma(a)\Gamma(b)} \sum_{n=0}^{\infty} \frac{\Gamma(a+n)\Gamma(b+n)}{\Gamma(c+n)} \frac{z^n}{n!} \quad (72)$$

and

$$F_2(\vec{\Omega}) = \frac{2}{\pi} \int_0^1 K_1(\vec{\rho}) H(\vec{\rho}, \vec{\Omega}) d\vec{\rho} \quad (73)$$

$$K_1(\vec{\rho}) = \begin{cases} \pi & |\vec{\rho}| \leq 0 \\ 2 \cos^{-1} \left( \frac{|\vec{\rho}|}{2} \right) - |\vec{\rho}| \sqrt{1 - \left( \frac{|\vec{\rho}|}{2} \right)^2} & 0 < |\vec{\rho}| < 2 \\ 0 & \text{otherwise} \end{cases} \quad (74)$$

$$H(\vec{\rho}, \vec{\Omega}) = \begin{cases} |\vec{\rho}|^{8/3} {}_2F_1 \left( \frac{-5}{6}, \frac{-5}{6}; 1; \frac{|\vec{\Omega}|^2}{|\vec{\rho}|^2} \right) & |\vec{\Omega}| \leq |\vec{\rho}| \\ |\vec{\rho}| |\vec{\Omega}|^{5/3} {}_2F_1 \left( \frac{-5}{6}, \frac{-5}{6}; 1; \frac{|\vec{\rho}|^2}{|\vec{\Omega}|^2} \right) & |\vec{\Omega}| \geq |\vec{\rho}| \end{cases} \quad (75)$$

### Appendix D. Development of the Lenslet SNR Ratio

This section provides a detailed development of the governing equation for the SNR within a single lenslet. The assumptions are that the detector array is an  $N \times N$  array of detectors, the detectors are centered about the origin, and that the photon arrival rate function is symmetric and centered at the origin. We begin with the standard equation for a linear estimation of the  $x$ -coordinate of the image centroid:

$$c_x = \frac{\sum_{i=1}^N \sum_{j=1}^N x_i (p_{ij} + n_{ij})}{\sum_{i=1}^N \sum_{j=1}^N (p_{ij} + n_{ij})}, \quad (76)$$

where  $c_x$  is the  $x$ -coordinate of the image centroid,  $x_i$  is the  $x$ -coordinate of the center of the  $i$ th column of detectors,  $p_{ij}$  is the signal count in the  $ij$ th detector, and  $n_{ij}$  is the noise in the  $ij$ th detector. We assume that  $p_{ij}$  is independent of  $p_{i'j'}$  when  $i \neq i'$  and  $j \neq j'$ , and that  $p_{ij}$  is independent of  $n_{i'j'}$ . The photon count,  $p_{ij}$  is a Poisson random variable with  $E[p_{ij}] = \lambda_{ij}$  where  $\lambda_{ij}$  is the photon arrival rate in the  $ij$ th detector. The read noise,  $n_{ij}$  is a zero mean Gaussian random process with standard deviation  $\sigma_e$ . We assume that

$$\sum_{i=1}^N \sum_{j=1}^N (p_{ij} + n_{ij}) = K, \quad (77)$$

where  $K$  is the total average arrival rate of photons within the entire lenslet. Also, if we assume that  $\lambda_{ij}$  is even symmetric, as is the case of a diffraction limited image, then

$$E[c_x] = \frac{\sum_{i=1}^N \sum_{j=1}^N x_i E[p_{ij}]}{K} = \frac{\sum_{i=1}^N \sum_{j=1}^N x_i \lambda_{ij}}{K} = 0. \quad (78)$$

In order to find an expression for the SNR, we must first solve for  $E[c_x^2]$ . Therefore,

$$E[c_x^2] = \frac{E \left[ \sum_{i=1}^N \sum_{j=1}^N \sum_{i'=1}^N \sum_{j'=1}^N x_i x_{i'} (p_{ij} + n_{ij})(p_{i'j'} + n_{i'j'}) \right]}{K^2}, \quad (79)$$

$$= \frac{\sum_{i=1}^N \sum_{j=1}^N \sum_{i'=1}^N \sum_{j'=1}^N x_i x_{i'} (E[p_{ij} p_{i'j'}] + E[n_{ij} n_{i'j'}])}{K^2}. \quad (80)$$

Let  $x_i = d\hat{x}_i$  where  $d$  is the width of a detector element, and  $\hat{x}_i$  is the normalized  $x$ -coordinate of the center of the  $i$ th column of detectors. Then,

$$E[c_x^2] = \frac{d^2 \sum_{i=1}^N \sum_{j=1}^N \sum_{i'=1}^N \sum_{j'=1}^N \hat{x}_i \hat{x}_{i'} (E[p_{ij} p_{i'j'}] + E[n_{ij} n_{i'j'}])}{K^2}, \quad (81)$$

$$= \frac{d^2}{K^2} \left( \sum_{i=1}^N \sum_{j=1}^N \hat{x}_i^2 E[p_{ij}^2] + \left( \sum_{i=1}^N \sum_{j=1}^N \hat{x}_i E[p_{ij}] \right)^2 - \sum_{i=1}^N \sum_{j=1}^N \hat{x}_i^2 E^2[p_{ij}] \right) + \frac{d^2}{K^2} \sum_{i=1}^N \sum_{j=1}^N \hat{x}_i^2 \sigma_e^2. \quad (82)$$

Applying Eqn. (78) to the second term of Eqn. (82) yields

$$E[c_x^2] = \frac{d^2}{K^2} \sum_{i=1}^N \sum_{j=1}^N \hat{x}_i^2 (E[p_{ij}^2] - E^2[p_{ij}]) + \frac{d^2}{K^2} N \sum_{i=1}^N \hat{x}_i^2 \sigma_e^2. \quad (83)$$

Also, since  $p_{ij}$  is a Poisson process,

$$E[p_{ij}^2] - E^2[p_{ij}] = \lambda_{ij}. \quad (84)$$

Substituting yields,

$$E[c_x^2] = \frac{d^2}{K^2} \sum_{i=1}^N \sum_{j=1}^N \hat{x}_i^2 \lambda_{ij} + \frac{d^2 N \sigma_e^2}{K^2} \sum_{i=1}^N \hat{x}_i^2, \quad (85)$$

$$= \frac{d^2}{K} \left( \sum_{i=1}^N \sum_{j=1}^N \hat{x}_i^2 \frac{\lambda_{ij}}{K} + \frac{N^2 \sigma_e^2}{K} \sum_{i=1}^N \frac{\hat{x}_i^2}{N} \right). \quad (86)$$

Now, because the  $x$  and  $y$  center locations are independent, we can write

$$E[c_x^2] + E[c_y^2] = \frac{d^2}{K} \left( 2 \sum_{i=1}^N \sum_{j=1}^N \hat{x}_i^2 \frac{\lambda_{ij}}{K} + \frac{2N^2 \sigma_e^2}{K} \sum_{i=1}^N \frac{\hat{x}_i^2}{N} \right). \quad (87)$$

We define the subaperture SNR

$$\text{SNR} = \sqrt{\frac{1}{E[c_x^2] + E[c_y^2]}}. \quad (88)$$

Therefore, the expression for SNR can be written as

$$\text{SNR} = \frac{K}{d\sqrt{2K \sum_{i=1}^N \sum_{j=1}^N \hat{x}_i^2 \frac{\lambda_{ij}}{K} + 2N^2\sigma_e^2 \sum_{i=1}^N \frac{\hat{x}_i^2}{N}}}. \quad (89)$$

In this research, our detector array is assumed to be of unit dimension, ranging from  $-\frac{1}{2}$  to  $\frac{1}{2}$  in both the  $x$  and  $y$  directions (therefore  $d = 0.25$ ). With this setup, and assuming a diffraction limited image within the lenslet, we find the expression for SNR becomes

$$\text{SNR} = \frac{K}{\sqrt{0.0346K + 2.5\sigma_e^2}}, \quad (90)$$

when the main lobe of the image is half the width of a detector, and

$$\text{SNR} = \frac{K}{\sqrt{0.0378K + 2.5\sigma_e^2}}, \quad (91)$$

when the main lobe of the image is the full width of a detector.

## Bibliography

1. Telephone interview with the Staff of the Starfire Optical Range, Phillips Laboratory, Kirtland Air Force Base, New Mexico, August 1995.
2. Angel, J., et al. "Adaptive Optics for Array Telescopes using Neural Network Techniques," *Nature*, 358:221-224 (15 November 1990).
3. Ellerbroek, B. "First-order performance evaluation of adaptive- optics systems for atmospheric-turbulence compensation in extended-field-of-view astronomical telescopes," *Journal of the Optical Society of America A*, 11:783-805 (February 1994).
4. Fried, D. L. "Optical resolution through a randomly inhomogeneous medium for very long and very short exposures," *Journal of the Optical Society of America*, 56:1372-1379 (1966).
5. Fugate, R. Q., et al. "Two generations of laser-guide-star adaptive-optics experiments at the Starfire Optical Range," *Journal of the Optical Society of America*, 11:310-324 (1994).
6. Jorgenson, M.B. and G.J. Aitken. "Evidence of a chaotic attractor in star-wander data," *Optics Letters*, 16:64-66 (15 January 1991).
7. Jorgenson, M.B. and G.J. Aitken, "Neural Network Prediction of Turbulence Induced Wavefront Degradations with Applications to Adaptive Optics." presented at SPIE - 1706, Orlando Florida, April 1992.
8. Jorgenson, M.B. and G.J. Aitken. "Prediction of atmospherically induced wave-front degradations," *Optics Letters*, 17:466-468 (1 April 1992).
9. Jorgenson, M.B. and G.J. Aitken, "Wavefront Prediction for Adaptive Optics." presented at ICO - 16, Active and Adaptive Optics, Garching Germany, August 1993.
10. Kay, S. M. *Modern Spectral Theory*. Englewood Cliffs, New Jersey: Prentice Hall, 1988.
11. Lloyd-Hart, M., et al., "A Neural Network Wavefront Sensor for Array Telescopes." presented at The International Commission for Optics, Florence, Italy, 1991.
12. Lloyd-Hart, M., et al., "First results of an on-line optics system with atmospheric wavefront sensing by an artificial neural network." accepted to the *Astrophysical Journal Letters*.
13. Miller, M., et al. "Characterization of atmospheric turbulence." *Proceedings of the SPIE/SPSE Technical Symposium East on Imaging Through the Atmosphere vol. 75*, 1977.
14. Pao, Y.H. *Adaptive Pattern Recognition and Neural Networks*. Reading, Massachusetts: Addison-Wesley, 1989.

15. Rogers, S.K. and M. Kabrisky. *An Introduction to Biological and Artificial Neural Networks for Pattern Recognition*. Bellingham, Washington: SPIE Optical Engineering Press, 1991.
16. Roggemann, M., et al., "Widening the effective field-of-view of adaptive optics telescopes using deconvolution from wavefront sensing: average and signal to noise ratio performance." submitted to the Journal of the Optical Society of America A.
17. Roggemann, M. C. "Optical performance of fully and partially compensated adaptive optics systems using least-squares and minimum variance phase reconstruction," *Comp. & Elec. Eng.*, 18:451-466 (1992).
18. Roggemann, M. C., et al. "Method for simulating atmospheric turbulence phase effects for multiple time slices and anisoplanatic conditions," *Applied Optics*, 34:4037-4051 (1995).
19. Rumelhart, D., et al. "Learning Internal Representations by Error Propagation." *Parallel Distributed Processing: Explorations in the Microstructures of Cognition 1*, chapter 8, 318-362, MIT Press, 1986.
20. Scharf, L. *Statistical Signal Processing*. Reading, Massachusetts: Addison-Wesley, 1991.
21. Tamura, S. and A. Waibel. "Noise reduction using connectionist models," *IEEE Transactions on Acoustics, Speech, and Signal Processing*, 1:553-556 (1988).
22. Troxel, S., et al. "Off-axis optical transfer function calculations in an adaptive-optics system by means of a diffraction calculation for weak index fluctuations," *Journal of the Optical Society of America A*, 11:2100-2111 (July 1994).
23. Tyler, G. A. "Merging: a new method for tomography through random media," *Journal of the Optical Society of America A*, 1:409-424 (1994).
24. Wallner, E. "Optimal wave-front correction using slope measurements," *Journal of the Optical Society of America*, 73:1771-1776 (December 1983).
25. Welsh, B.M. and C.S. Gardner. "Performance analysis of adaptive optics systems using laser guide stars and slope sensors," *Journal of the Optical Society of America A*, 1913-1923 (1989).
26. Welsh, B.M. and C.S. Gardner. "Effects of turbulence-induced anisoplanatism on the imaging performance of adaptive-astronomical telescopes using laser guide stars," *Journal of the Optical Society of America A*, 69-80 (1991).
27. Welsh, B.M. and M.C. Roggemann, "Evaluating the Performance of Adaptive Optical Telescopes." NATO Advanced Study Institute, Adaptive Optics for Astronomy, D. Alloin and J.-M. Mariotti editors, Kluwer Academic Publishers, pp. 211-226, 1993.
28. White, H. "Learning in Artificial Neural Networks: A Statistical Perspective," *Neural Computation*, 1:425-464 (1989).

29. Winnick, K. A. "Cramer-Rao lower bounds on the performance of charge-coupled-device optical position estimators," *Journal of the Optical Society of America A*, 3:1809-1815 (1986).
30. Wizinowich, P., et al. "Neural network adaptive optics for the Multiple Mirror Telescope," *SPIE Vol. 1542 Active and Adaptive Optical Systems*, 148-158 (1991).
31. Xue, Q., et al. "Neural-Network-Based adaptive matched filtering for QRS detection," *IEEE Transactions on Biomedical Engineering*, 39:317-329 (April 1992).

## *Vita*

Captain Dennis A. Montera [REDACTED] grew up throughout the Los Angeles, California area, and graduated from John F. Kennedy High School in 1984. He subsequently attended the United States Air Force Academy where he graduated on 1 June, 1988 with a Bachelor of Science in Electrical Engineering. He was commissioned into the United States Air Force on that same day. His first assignment was to Los Angeles AFB, California, where he served as a Project Engineer for the Deputy Chief of Staff, Developmental Planning. There he conducted system and architecture studies for advanced communications and missile warning satellites. In May 1991, he entered the Air Force Institute of Technology (AFIT). In 1992 he received a Master of Science in Electrical Engineering degree specializing in electro-optics, and was chosen to remain at AFIT to pursue his Ph.D. His doctoral research focuses on processing wavefront sensor slope measurements to improve adaptive optics performance.

[REDACTED]

REPORT DOCUMENTATION PAGE			Form Approved OMB No. 0704-0188	
Public reporting burden for this collection of information is estimated to average 1 hour per response, including the time for reviewing instructions, searching existing data sources, gathering and maintaining the data needed, and completing and reviewing the collection of information. Send comments regarding this burden estimate or any other aspect of this collection of information, including suggestions for reducing this burden, to Washington Headquarters Services, Directorate for Information Operations and Reports, 1215 Jefferson Davis Highway, Suite 1204, Arlington, VA 22202-4302, and to the Office of Management and Budget, Paperwork Reduction Project (0704-0188), Washington, DC 20503.				
1. AGENCY USE ONLY (Leave blank)	2. REPORT DATE 19 March 1996	3. REPORT TYPE AND DATES COVERED Dissertation		
4. TITLE AND SUBTITLE Linear and Non-Linear Preprocessing of Wavefront Sensor Slope Measurements for Improved Adaptive Optics Performance		5. FUNDING NUMBERS		
6. AUTHOR(S) Dennis A. Montera				
7. PERFORMING ORGANIZATION NAME(S) AND ADDRESS(ES) Department of Electrical and Computer Engineering, Air Force Institute of Technology, Wright-Patterson Air Force Base, Ohio 45433-7765		8. PERFORMING ORGANIZATION REPORT NUMBER		
9. SPONSORING / MONITORING AGENCY NAME(S) AND ADDRESS(ES)  Starfire Optical Range PL/LIG (Brent Ellerbroek) 3550 Aberdeen Ave SE Air Force Phillips Laboratory Kirtland Air Force Base, New Mexico 87117-5776		10. SPONSORING / MONITORING AGENCY REPORT NUMBER		
11. SUPPLEMENTARY NOTES				
12a. DISTRIBUTION / AVAILABILITY STATEMENT  Approved for public release, distribution unlimited		12b. DISTRIBUTION CODE		
13. ABSTRACT (Maximum 200 words) New methods for preprocessing wavefront sensor (WFS) slope measurements developed to improve the accuracy of WFS slope measurements, as well as estimating key atmospheric and system parameters from the slope signals. Both statistical and artificial neural network solutions are investigated. Also, new atmospheric models for generating slope and phase data with the proper spatial and temporal statistics are developed. The experiments in improving the accuracy of WFS slope measurements include reducing the WFS slope measurement error and compensating for adaptive optics system time delay through temporal slope prediction. The experiments in key parameter estimation include estimating the Fried coherence length, $r_0$ , the wind speed profile, the strengths of the atmospheric turbulence layers, and the WFS mean square slope estimation error. Results of the experiments are used to make generalized conclusions in several key areas: first, the types of useful information that can be extracted from the WFS slope measurements; second, a comparison of linear or non-linear methods; and third, the possibility of methods that can be developed which operate over useful ranges of seeing conditions. Overall, we find that simple transformations (either by neural network or statistical solution) on slope measurements can yield significant improvements in system accuracy without major changes to the adaptive optics system. Also, we find that both neural networks and statistical methods perform well when seeing conditions are fixed, and that viable solutions can be developed that operate over broad ranges of seeing conditions. In general, neural networks are much more robust when operating under variable seeing conditions than are the statistical solutions.				
14. SUBJECT TERMS adaptive optics, atmospheric optics, neural networks, wave front sensors,		15. NUMBER OF PAGES 103		
		16. PRICE CODE		
17. SECURITY CLASSIFICATION OF REPORT UNCLASSIFIED	18. SECURITY CLASSIFICATION OF THIS PAGE UNCLASSIFIED	19. SECURITY CLASSIFICATION OF ABSTRACT UNCLASSIFIED	20. LIMITATION OF ABSTRACT UL	